

Surface processes in the 7 November 2014 medicane from air-sea coupled high-resolution numerical modelling

Marie-Noëlle Bouin^{1,2}, Cindy Lebeaupin Brossier¹

¹CNRM, Université de Toulouse, Météo-France, CNRS, Toulouse, France

5 ²Laboratoire d'Océanographie Physique et Spatiale, Ifremer, University of Brest, CNRS, IRD, Brest, France

Correspondence to: Marie-Noëlle Bouin (marie-noelle.bouin@meteo.fr)

Abstract. A medicane, or Mediterranean cyclone with characteristics similar to tropical cyclones, is simulated using a kilometre-scale ocean-atmosphere coupled modelling platform. A first phase leads to strong convective precipitation, with high potential vorticity anomalies aloft due to an upper-level trough. Then, the deepening and tropical transition of the cyclone result from a synergy of baroclinic and diabatic processes. Heavy precipitation result from uplift of conditionally unstable air masses due to low-level convergence at sea. This convergence is enhanced by cold pools, resulting either from rain evaporation or from advection of continental air masses from North Africa. Backtrajectories show that air-sea heat exchanges moisten the low-level inflow towards the cyclone centre. However, the impact of ocean-atmosphere coupling on the cyclone track, intensity and lifecycle is very weak, due to a sea surface cooling one order of magnitude weaker than for tropical cyclones, even on the area of strong enthalpy fluxes. Surface currents have no impact. Analysing the surface enthalpy fluxes shows that evaporation is controlled mainly by the sea surface temperature and wind. Humidity and temperature at first level play a role during the development phase only. In contrast, the sensible heat transfer depends mainly on the temperature at first level throughout the medicane lifetime. This study shows that the tropical transition, in this case, is dependent on processes widespread in the Mediterranean Basin, like advection of continental air, rain evaporation and formation of cold pools, and dry air intrusion.

1 Introduction

Medicanes are small-size Mediterranean cyclones presenting, during their mature phase, characteristics similar to those of tropical cyclones including a cloudless and almost windless column at their centre looking like a cyclone eye, spiral rain bands and a large-scale cold anomaly surrounding a smaller warm anomaly at their centre, extending at least up to the mid troposphere (~400 hPa, Picornell et al., 2014). However, they differ from their tropical counterparts by many aspects: their intensity is much weaker, with maximum wind speed reaching those of tropical storms, or Category 1 hurricane on the Saffir–Simpson scale for the most intense of them (Miglietta et al., 2013); their radius ranges typically 50 to 200 km (Picornell et al., 2014); due to the enclosed character of the Mediterranean Sea leading rapidly to landfall, and to the limited ocean heat capacity, the duration of their mature phase vary from a few hours to 1 to 2 days; they are able to develop and sustain over sea surface temperature (SST) typically 15 to 23 °C (Tous and Romero, 2013), much colder than the 26 °C threshold of tropical cyclones (Trenberth, 2005; although tropical cyclones formed by a tropical transition can develop over colder water, McTaggart-Cowan et al. 2015); and a development phase including vertical wind shear and horizontal temperature gradient is necessary to the early stage of their development and the establishment of deep convection (e.g. Flaounas et al., 2015).

35 In the last decade, several studies documented their characteristics and conditions of formation, either from satellite observations (Tous and Romero, 2013), climatological studies (Flaounas et al., 2015), or case studies based on simulations (Miglietta et al., 2013; 2017; Miglietta and Rotunno, 2019). From these studies, a feature common to many medicanes is the

presence of an elongated upper-level trough (also known as a PV streamer) bringing cold air with high values of potential vorticity (PV) from higher-latitude regions. Other local effects favouring their development are: lee cyclones forming south of the Alps or north of the North African reliefs (Tibaldi et al., 1990); impact of the coastal reliefs in triggering deep convection; and relatively warm sea surface waters able to feed the process of latent heat release during their mature phase. Among Mediterranean cyclones, the classification of Hart (2003) established for tropical cyclones and adapted to the Mediterranean conditions (Picornell et al., 2014), helps to reliably identify warm core, symmetric events. It is nevertheless inadequate to describe the respective roles of upper-level and low-level processes (e.g. surface heat exchanges or role of geographical conditions like orographic lifting).

The medicane cases confirmed by converging characteristics as those mentioned above represent only a small portion of the Mediterranean cyclones (e.g. 13 over 200 cases of intense cyclones in the study of Flaounas et al., 2015, or roughly one per year). Due to this scarcity, isolating in a definite way the characteristics enabling to separate medicanes from other intense cyclones, with a slightly weaker upper-level and a stronger low-level PV anomalies (Flaounas et al., 2015). Recent comparative studies (e.g. Akhtar et al., 2014; Miglietta et al., 2017) showed a large diversity of duration, extension (size and vertical extent) and characteristics (dominating role of baroclinic versus diabatic processes) within the medicane category. Despite such a context, the role of the large-scale environment like the PV streamer and of the associated upper-level jet has been the subject of several studies. On a case study in September 2006, it was shown for the first time that the crossing of the upper-level jet by the cyclone to the left exit of the jet resulted in a rapid deepening of the surface low-pressure system by interaction between low-troposphere and upper-level PV anomalies (Chaboureaud et al., 2012). Recently, the ubiquitous presence of PV streamers and their key role in the baroclinic development of the medicanes have been confirmed by a study based on simulations and satellite analyses of several cases of intense medicanes (Miglietta et al., 2017). These studies emphasized the importance of the large-scale conditions prior to the development of the cyclone. They concluded also that, during their lifecycle, medicanes can rely either on purely diabatic processes or on a combination of baroclinic and diabatic processes (Miglietta and Rotunno, 2019).

Conversely, the investigation of the contribution of surface processes has motivated few studies so far. Some of them aimed at assessing the relative importance of surface heat extraction versus latent heat release and upper-level PV anomaly throughout the cyclone lifetime, by using adjoint models, factor separation techniques, or turning off selected processes in sensitivity experiments (Reed et al., 2001; Homar et al., 2003; Moscatello et al., 2008; Carrió et al., 2017). They concluded that, whereas the presence of the upper-level trough during the earlier stage of the cyclone and the latent heat release during its developing and mature phases are necessary to its deepening and maintenance, the role of surface heat fluxes is more elusive. Like in tropical cyclones, the latent heat fluxes always dominate the surface enthalpy processes, with sensible heat fluxes representing 25 to 30 % of the turbulent fluxes prior to the tropical transition, and 15 to 20 % during the mature phase (Pytharoulis, 2018). Early studies using simulations first concluded that low-level instability controlled by surface heat fluxes may be “an important factor of intensification” (Reed et al., 2001, case of January 1982) and that the latent heat extraction from the sea is a “key factor of feeding of the latent-heat release” (Homar et al., 2003, case study of September 1996). Turning off the surface turbulent fluxes during different phases of the cyclone brought contrast to this view, showing that the role of surface enthalpy in feeding the cyclonic circulation is not constant throughout its lifecycle. Indeed, it revealed important during its earliest and mature phases, playing only a marginal role during the deepening (Moscatello et al., 2008, case study of September 2006).

More recently, studies simulating several cyclones suggested that the impact of the surface fluxes on the cyclone are probably case-dependent (Tous and Romero, 2013; Miglietta and Rotunno, 2019). The latter study especially compared the

medicanes of October 1996 (between the Balearic Islands and Sardinia) and December 2005 (north of Libya) using the same
80 modelling platform. Sensitivity studies performed with and without surface fluxes showed contrasted results, which were
attributed to the different competing roles played by the WISHE-like mechanisms (Wind Induced Surface Heat Exchange:
Emanuel, 1986; Rotunno and Emanuel, 1987) versus baroclinic processes in the two cases. In both cases, high upper-level
PV values play a strong role in the initiation of the cyclone. The major difference comes from the role of surface fluxes. In
the case of October 1996, the cyclone warm core is formed by latent heat release fed at low level by heat and moisture
85 extracted from the sea. In the December 2005 case, the warm core is due to warm air seclusion. The authors concluded that
different categories of intensification mechanisms leading to medicanes co-exist. This suggests that mechanisms of transition
towards tropical-like cyclones are diverse, especially concerning the role of the air–sea heat exchanges.

As surface fluxes may strongly depend on the SST, a change of the oceanic surface conditions may, in theory, impact the
development of a medicane. Several sensitivity studies investigated the impact of a uniform SST change on the cyclone
90 development and lifecycle, for instance to anticipate the possible effect of the Mediterranean surface waters warming due to
climate change. Consistent tendencies were obtained on different case studies (Homar et al., 2003, case of September 1996;
Miglietta et al., 2011, case of September 2006; Pytharoulis, 2018, case of November 2014; Noyelle et al., 2019, case of
October 1996), showing that, as expected, warmer (respectively colder) SSTs lead to more (resp. less) intense cyclones.
However, changes of SST by less than ± 2 °C result in no significant change in the track, duration or intensity of the cyclone.

95 The impact of coupling atmospheric and oceanic models has been studied mainly using regional climate models on seasonal
to interannual time scales. Comparing coupled and non-coupled simulations using a regional climate model showed an
impact of the coupling provided the horizontal resolution of the model is at least 0.08° (Akhtar et al., 2014). This resolution
proved also necessary to reproduce in a realistic way the characteristic processes of medicanes, including warm cores, and
strong winds at low level. Coupled simulations resulted in more intense latent and sensible heat surface fluxes, contrasting
100 with what is usually obtained in tropical cyclones due to the strong cooling effect of the cyclone on the sea surface (Schade
and Emanuel, 1999; D'Asaro et al., 2007). This can be due to the use of a 1D ocean model and its limited ability to reproduce
the oceanic processes responsible of the cooling. The consideration about the resolution needed to observe an impact of the
surface processes was confirmed by the results of Gaertner et al. (2017), or Flaounas et al. (2018). Both studies compares
several simulations at the seasonal or interannual scale, both coupled and uncoupled and from several regional climate
105 modelling platforms. No clear impact of the coupling on the cyclones intensity was evidenced but the authors attributed this
lack of impact to the relatively low horizontal resolution of the coupled experiments, between 18 and 50 km. Finally, a case
study comparing higher-resolution (5 km) coupled and uncoupled simulations of the medicane of November 2011 showed no
strong impact of the surface coupling, with a weak decrease of the SST of 0.1 to 0.3°C and a difference of 2 hPa on the
minimum of SLP and 5 m s^{-1} on the surface wind speed (Ricchi et al., 2017). The impact of ocean–atmosphere coupling in
110 high-resolution ($\sim 1\text{--}2 \text{ km}$), convection-resolving models has, to the best of our knowledge, not been assessed yet.

In the present study, we assess the feedback of the ocean surface on the atmosphere of the medicane of November 2014 (also
known as Qendresa) over the Strait of Sicily and Ionian Sea using a kilometre-scale ocean–atmosphere coupled model. We
investigate the role of the surface processes, especially during the mature phase of the medicane, and we examine the role of
the different parameters (including SST) controlling these fluxes throughout the lifecycle of the cyclone.

115 A brief description of the medicane, and the description of the modelling tools and simulation strategy are given in Sect. 2. In
Section 3, the results of the reference simulation are used to describe the medicane characteristics and lifecycle with its
different phases and to present the impact of the coupling. The role of the surface conditions and mechanisms controlling the
air–sea fluxes are assessed during the different phases in Sect. 4. These results are discussed in Sect. 5, and some conclusions
are given.

The case study is the Qendresa medicane that affected the region of Sicily on 7 November 2014. It has been the subject of several studies based on simulations, either investigating the role of SST anomalies or the impact of uniform SST change (Pytharoulis, 2018), the respective role of upper-air instability, surface exchanges and latent heat release (Carrió et al., 2017) or the predictability of the event, depending on the initial conditions and horizontal resolution of the model (Cioni et al., 2018). All those studies showed that the predictability of this event and especially of its track is rather low, even with high horizontal (1–2 km) and vertical (50 to 80 levels) resolutions of present operational numerical weather prediction (NWP) platforms. A recent study based on the ensemble forecasts of the ECMWF (European Centre for Medium-Range Weather Forecasts, Di Muzio et al., 2019) showed that the predictability of occurrence (with respect to the operational analysis) is good as early as 7.5 days lead time, but the predictability of the position is weak, especially between 4 and 1 days lead time (their Fig. 6). The predicted central pressure is also consistently 10 to 14 hPa higher than the analysed one, whatever the lead time considered.

2.1 The 7 November 2014 medicane

On 5 and 6 November 2014, a PV streamer extended from Northern Europe to North Africa, bringing cold air (-23°C) and enhancing instability aloft. A general cyclonic circulation developed over the Western Mediterranean basin while Eastern Mediterranean was dominated by high pressures (Fig. 1a). At low level on 6 November, the cold and warm fronts associated with the baroclinic disturbance reinforced due to a northward advection of warmer and moist air, from North Africa (Fig. 1b). The system moved towards the Sicily Strait and deepened during the night of 6 to 7 November. On the early hours of 7 November, the upper-level PV trough and the low-level cyclone progressively aligned (Fig. 1c), reinforcing the PV transfer from above and the low-level instability. Strong convection developed, with heavy precipitation in the Sicily area. The low-level system rapidly deepened in the morning of 7 November, with a sudden drop of 8 hPa in 6 hours, and evolved to the quasi-circular structure of a tropical cyclone with spiral rain bands and a cloudless eye-like centre. The maximum intensity was reached around 12:00 UTC on 7 November north of Lampedusa (see Fig. 3 for main place names). The system drifted eastwards slowly weakening during the afternoon of the 7 November with a first landfall at Malta around 17:00 then moved northeastwards to reach the Sicilian coasts in the evening. It then continued its decay during the following night close to the Sicily coasts, and lost its circular shape and tropical cyclone appearance around 12:00 UTC on 8 November.

2.2 Simulations

Three numerical simulations of the event were performed using the state-of-the-art atmospheric model Meso-NH (Lac et al., 2018) and the oceanic model NEMO (Madec and the NEMO Team, 2016).

2.2.1 Atmospheric model

The non-hydrostatic French research model Meso-NH version 5.3.0 is used here with a fourth-order centered advection scheme for the momentum components and the piecewise parabolic method advection scheme from Colella and Woodward (1984) for the other variables, associated with a leapfrog time scheme. A C grid in the Arakawa convention (Mesinger and Arakawa, 1976) is used for both horizontal and vertical discretizations, with a conformal projection system of horizontal coordinates. A fourth-order diffusion scheme is applied to the fluctuations of the wind variables, which are defined as the departures from the large-scale values. The turbulence scheme (Cuxart et al., 2000) is based on a 1.5-order closure coming from the system of second-order equations for the turbulent moments derived from Redelsperger and Sommeria (1986) in a one-dimensional simplified form assuming that the horizontal gradients and turbulent fluxes are much smaller than their

vertical counterparts. The mixing length is parameterized according to Bougeault and Lacarrere (1989) who related it to the distance that a parcel with a given turbulent kinetic energy at level z can travel downwards or upwards before being stopped by buoyancy effects. Near the surface, these mixing lengths are modified according to Redelsperger et al. (2001) to match both the Monin–Obukhov similarity laws and the free-stream model constants. The radiative transfer is computed by solving long-wave and short-wave radiative transfers separately using the ECMWF operational radiation code (Morcrette, 1991). The surface fluxes are computed within the SURFEX module (Surface Externalisée, Masson et al., 2013) using over sea the iterative bulk parametrization ECUME (Belamari et al., 2005; Belamari and Pirani, 2007) linking the surface turbulent fluxes to the meteorological gradients and the SST through the appropriate transfer coefficients. The Meso-NH model shares its physical representation of parameters, including the surface fluxes parametrization, with the French operational model AROME (Seity et al., 2011) used for the Météo-France NWP with a current horizontal grid spacing of 1.3 km. In this configuration, deep convection is explicitly represented while shallow convection is parametrized using the eddy diffusivity Kain–Fritsch scheme (Pergaud et al., 2009).

In the present study, a first atmosphere-only simulation with a grid spacing of 4 km has been performed on a larger domain of $3200 \text{ km} \times 2300 \text{ km}$ (D1, see Fig. 2). This simulation started at 18:00 UTC the 6 November and lasted 42 h until 12:00 UTC the 8 November. Its initial and boundary conditions come from the ECMWF operational analyses every 6 h.

As described in the following, this 4 km simulation then provides initial and boundary conditions for simulations on a smaller domain of $900 \text{ km} \times 1280 \text{ km}$ (D2, Fig. 2). This domain extension was chosen as a trade-off between computing time and an extension large enough to represent the physical processes involved in the cyclone lifecycle, including the influence of the coasts. All simulations on the inner domain D2 share their horizontal grid (with resolution 1.33 km) and vertical grid with 55 stretched terrain-following levels, and a time step of 3 s. Atmospheric and surface parameter fields are issued every 30 minutes.

2.2.2 Oceanic model

The ocean model used is NEMO (version 3_6) (Madec and the NEMO Team, 2016) with physical parametrizations as follows. The total variance dissipation scheme is used for tracer advection in order to conserve energy and enstrophy (Barnier et al., 2006). The vertical diffusion follows the standard turbulent kinetic energy formulation of NEMO (Blanke and Delecluse, 1993). In case of unstable conditions, a higher diffusivity coefficient of $10 \text{ m}^2 \text{ s}^{-1}$ is applied (Lazar et al., 1999). The sea-surface height is a prognostic variable solved thanks to the filtered free-surface scheme of Roullet and Madec (2000). A no-slip lateral boundary condition is applied and the bottom friction is parameterized by a quadratic function with a coefficient depending on the 2D mean tidal energy (Lyard et al., 2006; Beuvier et al., 2012). The diffusion is applied along iso-neutral surfaces for the tracers using a Laplacian operator with the horizontal eddy diffusivity value ν_h of $30 \text{ m}^2 \text{ s}^{-1}$. For the dynamics, a bi-Laplacian operator is used with the horizontal viscosity coefficient η_h of $-1.10^9 \text{ m}^4 \text{ s}^{-1}$.

The configuration used here is sub-regional and eddy-resolving, with a $1/36^\circ$ horizontal resolution over an ORCA grid from 2.2 to 2.6 km resolution named SICIL36 (ORCA is a tripolar grid with variable resolution, Madec and Imbard, 1996), that was extracted from the MED36 configuration domain (Arsouze et al., 2013) and shares the same physical parametrizations with its “sister” configuration WMED36 (Lebeaupin Brossier et al., 2014; Rainaud et al., 2017). It uses 50 stretched z -levels in the vertical, with level thickness ranging from 1 m near the surface to 400 m at the sea bottom (i.e. around 4000 m depth) and a partial step representation of the bottom topography (Barnier et al., 2006). It has 4 open boundaries corresponding to those of the D2 domain shown in Figure 2, and its time step is set to 300 s. The initial and open boundary conditions come from the global $1/12^\circ$ resolution PSY2V4R4 daily analyses from Mercator Océan International (Lellouche et al., 2013).

2.2.3 Configuration of simulations

The three-hourly outputs of the large-scale simulation on D1 were used as boundary and initial conditions for 3 different simulations on the smaller domain D2, based on the atmospheric and oceanic configurations described previously. These three simulations start at 00:00 UTC on 7 November and last 36 h until 12:00 UTC on 8 November. The first atmosphere-only simulation called NOCPL used a fixed SST forcing, while the CPL simulation is the two-way coupled simulation between the Meso-NH and NEMO-SICIL36 model. Indeed, in CPL, the SURFEX-OASIS coupling interface (Voldoire et al., 2017) enables to exchange the SST and two-dimensional surface currents from NEMO to Meso-NH and the two components of the momentum flux, the solar and non-solar heat fluxes and the freshwater flux from Meso-NH to NEMO every 15 minutes. To test the respective impact of the surface currents on the atmosphere with respect to the impact of the SST, another coupled simulation has been performed (NOCUR in the following). It is similar to CPL except that the surface currents are not exported from NEMO to Meso-NH.

In order to ensure that the impact of the coupling in the NOCUR and CPL configurations corresponds to the time evolution of the SST rather than to a change in the initial SST field, the SST field (shown in Fig. 3) used as a surface forcing in NOCPL (and kept constant throughout the simulation) is the field produced by the CPL run, 1 h after the beginning of the simulation (i.e. after the initial adjustment of the oceanic model).

2.3 Validation

The tracks of Qendresa obtained in the three different simulations are compared to the best track based on observations (brightness temperature from radiance in the 10.8 μm channel measured by the SEVIRI instrument aboard the MSG satellite, see Cioni et al., 2018) in Figure 3. All the simulated tracks are shifted northwards with respect to the observations since the beginning of the simulations. The mean distance between the simulated and observed tracks is close to 85 km with no significant difference between the simulations. Cioni et al. (2018) showed that using horizontal resolutions finer than 2.5 km is mandatory to accurately represent the fine-scale structure of this cyclone and its time evolution. Sensitivity studies showed an increased convergence of simulated track towards the observations with higher resolution, the best agreement being obtained with a nested configuration and an inner domain at 300 m resolution. In the present study, several sensitivity tests based on these results were performed on the smaller-domain simulation to improve the simulated track: i) the starting time of the simulation was changed between 12:00 UTC on 6 November and 00:00 UTC on 7 November with increment of 3 h; ii) the number of vertical levels in Meso-NH was increased to 100, with a stretching ensuring a better sampling in the atmospheric boundary layer; iii) the atmospheric simulation was performed without nesting, initial and boundary conditions from ECMWF, and horizontal resolution of 2 km. Note that our inner domain D2 is close in its extension to the domain used by Cioni et al. (2018). None of these tests resulted in a significantly improved track, the northward shifting of the cyclone occurring in every case in the early hours of the 7 November.

The simulated cyclone nevertheless shows a deepening and maximum intensity close to the observed ones, even if a direct (i.e. co-localized) comparison is not possible due to the northward shift of its track. A strong deepening of almost 15 hPa is obtained in the first 12 h of the CPL simulation (Fig. 4b) with a minimum value at 12:30 UTC on the 7 November close to the minimum observed at Linosa station. This station has been chosen as the closest point to the best track from observations at the time of the observed maximum intensity of the storm. The surface wind speeds show peak values at the same time (Fig. 4a), and a time evolution in good agreement with METAR observations at the stations of Lampedusa, Pantelleria or Malta. Wind speed averaged over a 50 km radius around the cyclone centre presents a time evolution close to the control simulation of Cioni et al. (2018).

3 Medicane lifecycle and coupling impact

This part presents first the successive phases of the event based on an analysis of upper-level and mid-troposphere processes. Then, the impact of taking into account the short-time evolution of the SST on the atmospheric surface processes, through ocean–atmosphere coupling, is assessed.

240 3.1 Chronology of the simulated event

The successive phases of the medicane are examined using the methodology of Fita and Flaounas (2018) based on its upper-level and low-level dynamics, and on its asymmetry and thermal wind. Figure 5 shows the 300 hPa PV anomaly, SLP, surface wind and equivalent potential temperature θ_e at 850 hPa from the NOCPL simulation. Moreover, phase space diagrams are commonly used to describe in a synthetic way the symmetric characteristics of the cyclone, as well as the thermal characteristics and extent of its core. The present version in Figure 6 showing the evolution of Qendresa from 01:00 UTC on 7 November to 12:00 UTC on 8 November is derived from the original work of Hart (2003) using the adaptation of Picornell et al. (2014) for smaller-scale cyclones. The radius used for computing the low-troposphere thickness asymmetry B , the low-troposphere and upper-troposphere thermal winds ($-V_{TL}$ and $-V_{TU}$ respectively) has been fitted to the radius of maximum wind at 850 hPa and is close to 100 km, and the low troposphere and upper troposphere are defined here as the 925–700 hPa and 700–400 hPa levels respectively. Please note that the radius of maximum wind is ill defined or larger during the first stage of development of the cyclone, whereas it is steady and close to 90 km during the major part of its lifetime. As a result, the diagram obtained is probably not representative of the cyclone structure during its first hours.

At 06:00 UTC on 07 November, the PV streamer has moved northwards from Libya and is located south of the SLP minimum (Fig. 5a). A south-north cold front is clearly visible in the 850 hPa θ_e , east of the cyclone centre, and the medicane centre is located under the left exit of the upper-level jet (Fig. 5b). The minimum SLP starts to decrease to reach 985 hPa around 11:00 UTC, corresponding to a strong deepening rate of 1.4 hPa hr^{-1} for 10 hours. This phase corresponds also to the increase of the maximum wind at low level, and of the wind speed averaged over a 100 km radius around the cyclone centre (Fig. 4). It is referred to as “development phase” in the following. The heaviest rainfall are obtained during this phase (Fig. 7) with 10 h accumulated rain above 200 mm locally and instantaneous values above 50 mm h^{-1} east of Sicily and at sea between Pantelleria and Malta. As in Fita and Flaounas (2018), it also corresponds to the maximum thermal wind (Fig. 6).

The jet then moves further over the Ionian Sea and Sicily and the SLP minimum is aligned with the 300 hPa PV anomaly at 11:00 UTC on 7 November (Fig. 5c). It corresponds to the beginning of the “mature phase”, with a maximum intensity of the medicane around 12:00 UTC (Fig. 4). The medicane presents the circular shape typical of tropical cyclones with spiral rainbands, and a warm, symmetric core (Fig. 5d) extended up to 400 hPa (Fig. 6). The upper-level PV anomaly stays wrapped around the SLP until 17:00 UTC, and both structures drifts eastwards south of Italy (Fig. 5e). The medicane slowly decreases in intensity (Fig. 4) until its landfall in the southeast of Sicily at 18:00 UTC. The cold front drifts eastwards away of the cyclone centre, evolving eventually into an occluded front (Fig. 5f) wrapped around the SLP minimum. This mature phase, although the most intense of the cyclone, results in more scattered rainfall than the development phase (Fig. 7).

The cyclone then moves northeastwards towards the Ionian Sea and continuously decreases until 12:00 UTC on 8 November (“decay phase” hereafter). The SLP minimum steadily increases (Fig. 4), the upper-level PV anomaly has evolved into a cut-off and is still collocated with the cyclone centre (Fig. 5g). The 850 hPa warm core has extended $\sim 250 \text{ km}$ around the cyclone centre (Fig. 5h).

In the following, the possible impact of the ocean–atmosphere coupling on the cyclone intensity is examined by comparing the results of the CPL, NOCUR, and NOCPL simulations. The time period for this comparison is the 7 November only, as the medicane has lost a large part of its intensity in the evening of the 7 November.

3.2 SST evolution

Taking into account the effect of the SST cooling only (NOCUR) results in a slightly slower and less intense deepening by 1.5 hPa and almost no change of the maximum wind (Fig. 4). Including the effect of the surface currents on the atmospheric boundary layer results in a slightly more intense cyclone (1.5 hPa difference) at its maximum and 8 m s^{-1} stronger maximum wind. Figure 3 shows also that no significant difference on the track is obtained between the NOCPL, NOCUR and CPL simulations, except maybe when the cyclone centre loops east of Sicily at the end of the day. The median values of the difference of the SST between the CPL and NOCPL simulations over the whole domain, and the values of the 5 %, 25 %, 75 % and 95 % quantiles are shown Figure 8. This median surface cooling is very weak and reaches barely $0.1 \text{ }^{\circ}\text{C}$ at the end of the development phase, and is close to $0.2 \text{ }^{\circ}\text{C}$ at the beginning of the decay phase. Its further evolution, during the decay phase, is very weak with values of $0.25 \text{ }^{\circ}\text{C}$ at 23:00 UTC, on 07 November. The maximum cooling is $0.6 \text{ }^{\circ}\text{C}$. To focus on the effects of this surface cooling on the surface processes feeding the cyclone, we used a conditional sampling technique to isolate the areas with enthalpy flux above 600 W m^{-2} that corresponds to the mean value of the 80 % quantile of the enthalpy flux on the day of the 7 November. The enthalpy flux is defined here as the sum of latent heat flux LE and the sensible heat flux H . On this area (EF600 hereafter), the SST difference and its time evolution are slightly larger with a median difference of $-0.2 \text{ }^{\circ}\text{C}$ at the beginning of the mature phase and close to $-0.4 \text{ }^{\circ}\text{C}$ at the end of 7 November. The SST difference obtained in NOCUR on EF600 is slightly larger than in CPL but the difference is not significant. The SST cooling on the area of highest fluxes that are responsible for supplying the medicane in heat and moisture is therefore under $0.4 \text{ }^{\circ}\text{C}$ in median value, and much weaker than typical cooling values observed under tropical cyclones, that commonly reach 3 to $4 \text{ }^{\circ}\text{C}$ (e.g. Black and Dickey, 2008). In addition, the spatial extent of the cooling does not correspond to a clear wake as in tropical cyclones (not shown).

The conclusion of this part is that surface cooling under this medicane is one order of magnitude smaller than what is obtained under tropical cyclone, with no significant impact of the surface currents. Quantifying the surface cooling under other medicanes could lead to contrasting results. For instance, in an ocean–atmosphere–waves coupled simulation of a strong storm in the Gulf of Lion, surface cooling of $2 \text{ }^{\circ}\text{C}$ was obtained (Renault et al., 2012). Such a discrepancy with a storm of comparable intensity cannot be explained easily, and this is beyond the scope of the present work. A possible explanation could be the storm track affecting the same place by making a loop in the Gulf of Lion, resulting in a larger cooling. The difference can also come from a different oceanic preconditioning (their case occurred in May), with stronger stratification or a shallower mixed layer in the Gulf of Lion that amplifies cooling due to mixing/entrainment process.

3.3 Impact on turbulent surface exchanges

A comparison of the time evolution of the enthalpy flux, sensible and latent heat fluxes of the NOCPL and CPL simulations shows that the differences are very weak even on the EF600 area (Fig. 9a). During the decay phase where it is maximum, the mean difference of the enthalpy flux is 25 W m^{-2} , with a standard deviation of 13 W m^{-2} . Compared to the values of the turbulent fluxes on this area, between 500 and 800 W m^{-2} for LE and 100 and 250 W m^{-2} for H , this value is weak. Expressed in percent of the fluxes values, the relative difference is close to 2 % at the beginning of the mature phase and reaches 5 % at 21:00 UTC on 7 November, when the medicane has weakened. The relative difference of the sensible heat flux varies between 4 and 10 % due to the lower values of H , and the value of the difference is close to 7 W m^{-2} with a standard

deviation of 4 W m^{-2} . So, coupling appears to have a very weak impact on the turbulent heat fluxes even in the EF600 area. Again, the effect of the surface currents (CPL versus NOCUR in Fig. 9b) is not significant.

In the following, except if otherwise specified, the results of the NOCPL simulation are used to investigate the medicane behaviour, focusing on what occurred area of interest (AI in Fig. 2).

4 Role of surface fluxes and mechanisms

This section investigates the role of the surface parameters in controlling the surface heat fluxes during the different phases of the medicane. The objective is to assess the relative role of the SST, the surface wind, and the heat and moisture in the surface layer in the surface heat transfer and its time evolution.

4.1 Representation of surface fluxes and methods

In numerical atmospheric models, the turbulent heat fluxes are classically computed as a function of surface parameters using bulk formulae:

$$H = \rho c_p C_h \Delta U \Delta \theta \quad (1)$$

$$LE = \rho L_v C_e \Delta U \Delta q \quad (2)$$

with the air density, c_p the air thermal capacity and L_v the vaporization heat constant, ΔU , $\Delta \theta$ and Δq the wind speed at first level with respect to the sea surface, the difference between the SST and the potential temperature at first level, and the difference between the specific humidity at saturation with temperature equal to SST and the specific humidity at first level, respectively. The transfer coefficients C_h and C_e are defined as

$$C_h^{1/2} = \frac{C_{hn}^{1/2}}{1 - \frac{C_{hn}^{1/2}}{\kappa} \psi_T(z/L)} \quad (3)$$

and

$$C_e^{1/2} = \frac{C_{en}^{1/2}}{1 - \frac{C_{en}^{1/2}}{\kappa} \psi_q(z/L)} \quad (4)$$

with κ the von Karman's constant, ψ_T and ψ_q empirical functions describing the stability dependence, C_{hn} and C_{en} the neutral transfer coefficient for heat and moisture and L the Obukhov length (which depends, in turn, on the virtual potential temperature at first level and on the friction velocity u_*). In the ECUME parameterization used in this study, the neutral transfer coefficients C_{hn} and C_{en} are defined as polynomial functions of the 10 m neutral wind speed.

The transfer coefficients depends on the wind speed at 10 m and on the Obukhov length through the stability functions. The Obukhov length is expressed as in Liu et al. (1979):

$$L = - \frac{T_v^2 u_*^2}{\kappa g T_{v*}} \quad (5)$$

with T_v the virtual temperature at the first level, depending on the temperature and specific humidity, and T_{v*} the scale parameter for virtual temperature depending on the temperature and humidity at the first level. As a consequence, the transfer coefficients depend as the fluxes on the wind speed, on the temperature and specific humidity at the first level, and on the SST. In the following, we do not distinguish between the temperature and potential temperature at first level.

The time evolution of the median values, and 5 %, 25 %, 75 % and 95 % quantiles of the latent and sensible heat fluxes is shown in Figure 10a for the 7 November, on the EF600 area, and the time evolution of the median values and quantiles of

the SST in Figure 10b. The latent heat flux is always much higher than the sensible heat flux, as this is generally the case at sea when the SST is above 15 °C (e.g. Reale and Atlas, 2001). The sensible heat flux represents here 22 % of the total turbulent flux during the development phase, 12 to 15 % during the decay phase. Both fluxes show asymmetric distributions with upper tail (95 %) more distant from the median than the lower tail (5 %). This is partly due to the conditional sampling ($LE + H > 600 \text{ W m}^{-2}$) used here, as low fluxes are cut off by the sampling. The median value of H is maximum at the end of the development phase (180 W m^{-2} at 08:00 UTC), while the maximum value of its 95 % quantile is reached at the beginning of the development phase (332 W m^{-2} at 04:00 UTC). During the mature phase, both the median and 95 % quantile values of H are continuously decreasing. Conversely, the maximum of the median value of LE (635 W m^{-2}) is reached at 09:00 UTC during the development phase and stays approximately constant until 15:00 UTC. The maximum of the 95 % quantile (845 W m^{-2}) is reached at the end of the development phase. The decrease of LE starts later than the for H (around 15:00, as the system has started to weaken) and is slower until the end of the 7 November. The median values of LE in this EF600 sampling are constant or slightly increasing until the evening (20:00 UTC), whereas the minimum values (5 % quantile) increase continuously until the end of the day. Again, this is probably partly due to the sampling used here.

The time evolution of the median values and quantiles of the SST shows, conversely, asymmetric distributions with lower tails much longer than upper tails (Fig. 10b). The maximum values of SST (95 % quantile) are almost constant with time and close to 24 °C, while the lower and median values vary due to the conditional sampling EF600 and the motion of the cyclone away from the warm SST area.

To investigate the mutual dependencies and co-variabilities of the fluxes and parameters listed above, we used the rank correlation of Spearman, which corresponds to the Pearson or linear correlation between the rank of the two variables in their respective sampling (Myers et al., 2010). This metrics enables relating monotonically rather than linearly the variables of interest and is more appropriate in the case of non-linear relationships as this is the case for the fluxes that may be related to the variables additionally through the transfer coefficients.

The co-variabilities are analysed first in the whole domain, to determine what contributes the most to the fluxes globally, then in the EF600 area to isolate processes explicitly responsible for the fluxes contributing the most to the growth and maturity of the medicane. The corresponding values are given in Tables 1 to 3 for the EF600 area, and for 3 time periods considered representative of the development, mature and decay phases respectively, i.e. 09:00, 13:00 and 18:00 UTC on 7 November.

4.2 Development phase

At low level, this phase corresponds to a low-pressure system resulting of the evolution of the instability generated by the lee cyclone induced by the North African relief, with strong baroclinic structures. The heavy precipitation obtained during the first hours are co-localized with frontal structures. A warm sector is present at the east of the domain, with a cold front extending south-east from the south of Italy and very strong low-level convergence between a southeasterly flow in the warm sector and a south to southwesterly flow in the cold sector.

At 08:30 UTC on 7 November (Fig. 11), strong convergence lines are present between Sicily and Tunisia, close to the cyclonic centre. The low-level virtual potential temperature θ_v superimposed to the equivalent potential temperature θ_e on the map (Fig. 11a) and on an east-west (E-W) cross section close to the SLP minimum (Fig. 11b) is used here as a marker of cold pools (with an upper limit of 19°C for θ_v – Ducrocq et al., 2008; Bresson et al., 2012). Some of these cold pools are the result of evaporating processes under convective precipitation, while those located at sea along the North African coast originates from dry and cold air advected from inland (the discrimination between these two kinds of cold pools was done using a simulation without the latent heat transfer due to rain evaporation, not shown here). The cold and moist air spreads to the

385 surface following density currents and is advected northwestwards by the low-level flow. On the west and south of the domain, cold pools were formed at night by radiative processes over land, then advected over sea with a vertical extent of ~ 1000 m (see the westernmost part of the W-E transect, Fig. 11b).

The strong horizontal convergence at low level, leading to uplift and deep convection on air masses with high θ_e , is located on the upwind edge of the cold pools. During this development phase, the cold pools located in the southerly flow move
390 northwards, towards the centre of the cyclone and trigger convection up to 3000 m of the northwesterly low-level flow with high θ_e (Fig. 11b). This propagates the surface warm anomaly close to the cyclone centre (now located under the 300 hPa PV anomaly) up to 3000 m and develops a corresponding low- to mid-troposphere PV anomaly. At the same time, a dry air intrusion from the upper levels brings air masses with low θ_e and relative humidity below 20 % to 3000 m, resulting in a upper-to-mid-troposphere PV anomaly (Fig. 15a and c).

395 To identify the surface parameters controlling evaporation at sea, the time evolution of the Spearman's rank correlations between the latent heat flux, U_{10} , θ , the SST and q is given Figure 12 and Tables 1 to 3.

During this phase, on the whole domain, the controlling parameters for LE are the SST and the wind (positively correlated), the specific humidity (negatively) and the potential temperature (negatively). Potential temperature and humidity are also strongly positively correlated ($r_s = 0.55$ over the whole domain), due to the advection of cold and dry air by the southerly
400 low-level flow from the Tunisian and Libyan continental surface (Fig. 13b, c and f, at 09:00 UTC). This air mass progressively charges itself in heat and moisture on the area of strongest enthalpy fluxes north of the Libyan coasts (Fig. 13a). The EF600 area of strong fluxes and cold/dry air corresponds also to the area of warm SST (Fig. 13e). Within this area, the main influence on LE is from the wind, then from the SST (Fig. 12b, Table 1). There is no effect of the potential temperature (weak or negative correlations, Fig. 12b, Table 1) and a weak effect of the specific humidity.

405 LE is always much higher than H (Fig. 10a), resulting in the “strong flux area” EF600 being determined by LE values rather than H values, and more homogeneous values of LE than H over this area. However, H can reach strong values locally with respect to the LE during this development phase. As a consequence, values of H still show strong contrast on the EF600 area (Fig. 13d). During this development phase, it is controlled mainly by the potential temperature at first level (Fig. 14), partly indirectly through the stratification and transfer coefficient (not shown). On the EF600 area also, the SST influence is weak
410 at all times, the major control is also from the potential temperature ($r_s = -0.70$ at 09:00 UTC). The wind plays a secondary role. The enhanced control by the potential temperature is partly due to the continental air masses advected from North Africa, and partly to the presence of the cold pools under the areas of deep convection and strong wind. The H values are located offshore of the Tunisian and Libya coasts downwind of the strong low-level flow bringing cold air from the continent.

415 4.3 Mature phase

At 13:00 on 7 November, the PV anomalies at 700 hPa and 300 hPa are aligned (Fig. 15c, e). A zonal cross section on the SLP minimum shows that a low-level PV anomaly with values above 5 PVU has formed around the centre of cyclone, extending from the surface up to the 300 hPa anomaly (Fig. 15). The warm core of the systems extends up to 850 hPa (Fig. 15a), and is limited upward by colder air (low θ_e) brought from aloft. The tangential velocity field shows low-level
420 convergence (up to 800 hPa) towards the cyclone centre, deep convection close to the centre, but no or very weak divergence at mid to upper troposphere. The cyclonic circulation has reinforced with horizontal wind speed above 8 m s^{-1} at all heights out of a radius of 10 km around the cyclone centre.

During this phase as the previous one, over the whole domain as in the EF600 area, the dominant role in controlling evaporation is played by the SST with an effect equivalent to the wind speed, and a decreasing influence of the humidity

425 (Fig. 12, Table 2). The area EF600 extends further north, closer to the cyclone centre, away from the area of cold and dry low-level air, which also tends to warm and moisten under the combined impact of the diurnal warming of the continental surfaces (not shown) and of the strong enthalpy fluxes offshore (Fig. 16a, c and f). The sensible heat flux is still controlled by the temperature, with an increasing influence of the wind.

4.4 Decay phase

430 In the afternoon of the 7 November, the cyclone first moves towards colder SSTs in the east of the Sicily Strait (Fig. 3), then crosses Sicily and reach the Ionian Sea around 20:00 UTC, with even colder SSTs, before slowly decaying and losing its tropical-like characteristics. To check the role played by warm and moist air extraction from the sea-surface in feeding the cyclone centre by air masses with high θ_e values, backtrajectories were used starting at 23:00 on the 7 November, south of the cyclone centre (Schär and Wernli, 1993; Gheusi and Stein, 2005). The trajectories of three air parcels originating from
435 very different places and arriving at the same place, at three vertical levels surrounding the level closest to 1500 m, are shown in Fig. 17. Their equivalent potential temperature ranges from 31 to 38 °C at their first appearance in the domain and is close to 45 °C on average when they reach their final point. On their trajectories, θ_e increases almost continuously, with a strong jump during their transit at low level (below 500 m) above the sea in the EF600 area (white contour in Fig. 17). A separate analysis of the two different stages of the trajectories has been performed. Stage 1 corresponds to the particles in the
440 low-level flow (between 200 and 1200 m above sea level) south and east of Sicily and stage 2 to their convective ascent from ~ 300 m to 1500 m. During stage 1, the potential temperature of the particles decreases of 1 °C in average while the mixing ratio increases of 2.8 g kg⁻¹. This shows that the increase in θ_e is due to strong surface evaporation. During stage 2, the mixed ratio of the particles decreases of 2 g kg⁻¹ and their potential temperature increases of 4.1 °C. This indicates condensation and latent heating. This demonstrates the strong role of the sea surface in increasing the moisture and heat of the low-level flow
445 before its approach of the cyclone centre, and of diabatic processes in reinforcing its warm core.

During the decay phase, the influence of the humidity on the evaporation, in the whole domain is weak (Fig. 12a). The area of strong enthalpy fluxes is still located on warm SSTs on the south of the domain (Fig. 18a, e), which is also the place of the strongest winds on the right-hand side of the cyclone (Fig. 18b). Within the EF600 area, there is almost no influence of the temperature or humidity on LE (Table 3). The influence of the wind speed is decreasing, the role of the SST is strong until
450 21:00 UTC when the cyclone reaches the northern Ionian Sea where the SST is much colder, and the effect of the wind speed becomes dominant at the very end (Fig. 12b). Concerning the sensible heat flux, there are less patches of strong flux corresponding to cold pools and low θ , but a medium-scale northwest–southeast gradient of H over the EF600 area, related to a NS gradient of wind speed (Fig. 18b). On the north of the EF600 area (where the wind speed is also the highest), the potential temperature is colder and H values are maximum.

455 In summary, at the scale of the domain, the latent heat flux (evaporation) is controlled by the SST and wind throughout the day of the 7 November: both strong winds (in the cold sector during the development phase, then close to the cyclone centre and in its right side) and warm SSTs (in the south of the domain) are thus necessary to have strong latent heat fluxes. Within the area where the turbulent fluxes are high (and where winds are strong and SSTs high), the control of evaporation is mainly from the wind (development and mature phases) then from the SST (decay phase). In contrast, the sensible heat flux is
460 always mainly controlled by the potential temperature in the surface layer. Colder air masses result in enhanced sensible heat flux, rather than strong wind or warmer SST. During the two first phases, this cold air is either advected from North Africa or created by evaporation under convective precipitation (cold pools). During the decay phase, strong latent heat transfer over warm SSTs warms the near-surface atmospheric layer and results finally in lower sensible heat transfer.

5 Discussion and conclusion

465 The comparison of the simulations with and without ocean coupling shows no significant impact of the evolution of the SST on the track, intensity or lifecycle of the medicane. The weak SST cooling, notably during the first 24 h of the simulation, is likely responsible for that. On the strong flux area, where the enthalpy flux feeds the cyclone in heat and moisture maintaining the convection and the latent heat release mechanism, the median value of the SST cooling is 0.2°C during the mature phase, and reaches barely 0.4°C at the end of the day. The median difference on H is -7 W m^{-2} during the mature phase, -12 W m^{-2} at 23:00 UTC on the 7 November (representing less than 10 % difference), and -19 W m^{-2} , -37 W m^{-2} on LE at the same two time periods (representing less than 5 % difference). Coupling with the surface currents has no significant impact of the simulation.

The co-variabilities of surface fluxes and parameters show nevertheless that, in this specific case, the SST exerts a strong control on the latent heat flux that dominates the surface heat transfer, throughout the whole duration of the event. During its development phase, there is also a strong influence of peculiarities of the Central Mediterranean: the transition between deep convection and heavy precipitation associated with baroclinic processes and the tropical-like cyclone takes place downwind of the low-level flow of dry and cold air originated from North Africa. These air masses with low θ_v encounter moist and warm air resulting of the strong sea-surface evaporation and enhance the deep convection at sea, together with the cold pools formed by rain evaporation and downdrafts. These cold pools of various origins displace the deep convection at sea. Uplift of warm air masses increases the low-level PV, and reinforces the vortex, which is moved northeastwards closer to the PV anomaly aloft.

It has recently been suggested that medicanes could be sorted into two (possibly three) different categories according to the intensity and role of air–sea heat exchanges and to the related surface mechanisms (Miglietta and Rotunno, 2019). The main difference between these two categories is the processes leading to the warm core of the cyclone. The first category corresponds to purely WISHE-like mechanisms, with latent heat release fed by heat and moisture extracted from the sea surface as processes responsible for the medicane deepening and warm-core building. The cyclone is detached from any large-scale, baroclinic structure during its mature phase, with no transfer of PV from the upper-level jet. The PV anomaly at all levels consists in: wet potential vorticity (WPV) produced diabatically by latent heat release (Eq. 4 in Miglietta et al., 2017) and dry potential vorticity (DPV) brought by intrusion of stratospheric air into the upper troposphere (their Eq. 3). Levels up to $\sim 600\text{ hPa}$ present a maximum of WPV due to latent heating, while DPV is almost constant up to $\sim 400\text{ hPa}$ where it increases sharply, and there is no real PV tower around the cyclone centre. The features characteristics of tropical cyclones are well marked: warm core extending up to 800 hPa , symmetry, low-level convergence and upper-level divergence, and strong contrast of θ_e ($\sim 8^{\circ}\text{C}$) between the surface and 900 hPa as an evidence of latent heating. The case of October 1996 chosen to represent this category shows very strong surface fluxes (above 1500 W m^{-2} over large areas) due to strong, persistent winds of orographic origin bringing cold and dry air for several days prior to the cyclone development, also contributing to destabilize the surface layer.

Medicanes of the second category also present similarities with tropical cyclones, like deep warm core and symmetrical wind field, but present both diabatic and baroclinic processes throughout their lifetime. The cyclone stays within a large-scale baroclinic environment, with the PV streamer slowly evolving into a cut-off low. The tropical-like features are less evident: weaker warm core, weaker gradient of θ_e ($\sim 3\text{--}4^{\circ}\text{C}$) between the surface and 900 hPa . Around the cyclone centre, a PV tower forms, with weak contrast between the DPV and WPV profiles. As an example, the warm core of the December 2005 medicane is not due to convective latent heating but to seclusion of warm air by colder air masses and extends up to 400 hPa . The surface enthalpy fluxes play only a marginal role and take maximum values of 1000 W m^{-2} for a few hours.

In the present case of Qendresa, strong air–sea exchanges at the surface and latent heat release act at building the warm core anomaly, as seen in Sect. 4.3 and 4.4. The surface enthalpy fluxes take intermediate values with maximum above 1500 W m^{-2} for a few hours on areas with warm SST and strong winds downwind of the dry low-level flow from North Africa. Thermal features characteristic of tropical cyclones are present, like low-level cold air advection from the south to the east, and warm air advection from the south to the north (Reale and Atlas, 2001), and the gradient of θ_e between the surface and 900 hPa takes intermediate values of $6\text{--}7^\circ\text{C}$. The wrapping of the PV streamer around the cyclone centre evolves into an upper-level cut-off at the end of the decay phase. Conversely, some typical features are not present: even if there is weak low-level convergence around the cyclone centre, no divergence is obtained at upper level. The area of maximum latent heat flux within the EF600 area is more controlled by the SST than by the wind speed (Fig. 12b and 13a, b, and e). No minimum of potential temperature or potential vorticity develop at 300 hPa close to the cyclone centre during the mature phase, as a marker of the PV anomaly erosion by the convective activity, and the upper-level PV anomaly never completely detaches from the large scale structure.

The vertical profiles of PV, DPV and WPV (defined as in Miglietta et al., (2017)) averaged on a 100 km radius circle around the cyclone centre show a minimum of WPV between 700 and 400 hPa during the decay phase, and a clear difference between DPV and WPV at low level (Fig. 19). The DPV is weak up to the mid troposphere and increases sharply above 400 hPa. The WPV anomaly at low levels that develop up to 700 hPa during the development phase is increased but its vertical extent is reduced to 800 hPa during the mature phase (13:00 UTC – see also Fig. 15e). This is due to a dry air intrusion during the mature and decay phases, which is limited downwards to mid troposphere because of this warm core (Fig. 15a). At the beginning of the decay phase, at 18:00 UTC, the latent heating within the cyclone core increases the WPV at low level and erodes the dry and cold (θ_e) air masses up to 650 hPa. The warm core and WPV anomaly extend upwards (Fig 15b, f), and the DPV anomaly is pushed up to 700 hPa (Fig. 15c, d).

This suggests that the medicane of November 2014 as simulated in this study presents characteristics close to an extratropical cyclone, or medicane of the second category as in Miglietta and Rotunno (2019). Its development phase is triggered by a PV streamer bringing instability at upper level, and baroclinic processes followed by strong convection at sea enhanced and maintained by cold pools due to rain evaporation at low level or by advection of dry and cold air from North Africa. Conjunction of advection of continental air masses with evaporation under storms has not been identified as leading to tropical transition of Mediterranean cyclones so far, even though it is probably rather ubiquitous, as both are rather widespread phenomena in the Mediterranean. Surface fluxes are strong and contribute to enhance the convection potential till the mature phase of the cyclone. Evaporation is mainly controlled by the SST and by the wind speed during the whole event, while the temperature difference between the SST and the cold air advected from North Africa during the development and mature phase play a strong role during its development. The vertical development of the warm core is limited, at the beginning of the decay phase, by a dry air intrusion that does not reach the lowest levels of the troposphere. Dry air intrusions have been recognized as common processes in Mediterranean cyclones by Flaounas et al. (2015) but their role in the cyclone lifecycle was not clearly assessed. Here, we suggest that they can act at limiting the extent of the convection at the beginning of the mature phase. The convective activity is stronger during the development than during the mature phase of the cyclone, resulting in heavy rainfall 12 to 6 h before the maximum wind speed, in consistency with previous studies of medicanes based on observations (Miglietta et al., 2013; Dafis et al., 2018). Finally, these results are consistent with those of Carrió et al. (2017). By using a factor separation technique, they show that while the role of the upper-level PV anomaly is crucial in preconditioning the event, its rapid deepening is due to the synergy of latent heat release and upper-level dynamics.

545 Coupling the atmospheric model with a 3D high-resolution oceanic model shows that the surface cooling susceptible to affect the surface fluxes is too weak in that case to impact the atmospheric destabilization processes at low level. Nevertheless, the effect of the medicane on the oceanic surface layer is probably significant. To better understand the sea surface evolution and the role of coupling, the ocean mixed layer response to the medicane and the mechanisms involved will be investigated in more details in future work.

550 **Author contributions.** MNB and CLB designed the simulations. MNB performed the simulations. Both authors interpreted the results and wrote the paper.

Competing interests. The author declare that they have no conflict of interest.

Acknowledgments

555 This work is a contribution to the HyMeX program (Hydrological cycle in the Mediterranean EXperiment - <http://www.hymex.org>) through INSU-MISTRALS support. The authors acknowledge the Pôle de Calcul et de Données Marines for the DATARMOR facilities (storage, data access, computational resources). The authors acknowledge the MISTRALS/HyMeX database teams (ESPRI/IPSL and SEDOO/OMP) for their help in accessing to the surface weather station data. The PSY2V4R4 daily analyses were made available by the Copernicus Marine Environment Monitoring Service
560 (<http://marine.copernicus.eu>). The ERA5 reanalysis at hourly timescales (doi: 10.24381/cds.bd0915c6) are produced by the European Centre for Medium-Range Weather Forecasts (ECMWF) and made available by the Copernicus Climate Change Service (<https://cds.climate.copernicus.eu>). METAR observations of SLP and wind were retrieved through the Weather Wunderground portal <https://www.wunderground.com>. The authors thank J.-L. Redelsperger (LOPS) for valuable discussions. We also thank E. Flaounas and an anonymous reviewer whose comments helped to greatly improve this paper.

565 References

- Akhtar, N., Brauch, J., Dobler, A., Béranger, K. and Ahrens, B.: Medicanes in an ocean–atmosphere coupled regional climate model, *Nat. Hazards Earth Syst. Sci*, 14, 2189–2201, 2014.
- 570 Arsouze, T., Beuvier, J., Béranger, K., Somot, S., Lebeaupin Brossier, C., Bourdallé-Badie, R., Sevault, F., and Drillet, Y.: Sensibility analysis of the Western Mediterranean Transition inferred by four companion simulations, *The Mediterranean Science Commission*, Monaco, in *Proceedings of the 40th CIESM Congress*, November 2013, Marseille, France, 2013.
- Barnier, B., Madec, G., Penduff, T., Molines, J.-M., Treguier, A.-M., Le Sommer, J., Beckmann, A., Biastoch, A., Böning, C., Dengg, J., Derval, C., Durand, E., Gulev, S., Remy, E., Talandier, C., Theetten, S., Maltrud, M., McClean, J., and De Cuevas, B.: Impact of partial steps and momentum advection schemes in a global ocean circulation model at eddy-permitting resolution. *Ocean Dyn.* 56 (5), 543–567, <https://doi.org/10.1007/s10236-006-0082-1>, 2006.
- 575 Belamari, S.: Report on uncertainty estimates of an optimal bulk formulation for surface turbulent fluxes, *Marine EnviRonment and Security for the European Area–Integrated Project (MERSEA IP)*, Deliverable D, 4, 2005.
- Belamari, S. and Pirani, A.: Validation of the optimal heat and momentum fluxes using the ORCA2-LIM global ocean-ice model, *Marine EnviRonment and Security for the European Area–Integrated Project (MERSEA IP)*, Deliverable D, 4, 2007.

- 580 Beuvier, J., Béranger, K., Lebeaupin Brossier, C., Somot, S., Sevault, F., Drillet, Y., Bourdallé-Badie, R., Ferry, N., and
Lyard, F.: Spreading of the Western Mediterranean deep water after winter 2005: time scales and deep cyclone transport,
J. Geophys. Res.: Oceans 117 (C7), <https://doi.org/10.1029/2011JC007679>. C07022, 2012.
- Black, W. J., and Dickey, T.D.: Observations and analyses of upper ocean responses to tropical storms and hurricanes in the
vicinity of Bermuda, J. Geophys. Res., 113, C08009, doi:10.1029/2007JC004358, 2008.
- 585 Blanke, B., and Delecluse, P.: Variability of the tropical Atlantic Ocean simulated by a general circulation model with two
different mixed-layer physics. J. Phys. Oceanogr. 23 (7), 1363–1388. <https://doi.org/10.1175/1520-0485023<1363:VOTTAO>2.0.CO;2>, 1993.
- Bougeault, P. and Lacarrère, P.: Parameterization of Orography-Induced Turbulence in a Mesobeta-Scale Model. Mon.
Weather Rev., 117, 1872–1890. [https://doi.org/10.1175/1520-0493\(1989\)117<1872:POOITI>2.0.CO;2](https://doi.org/10.1175/1520-0493(1989)117<1872:POOITI>2.0.CO;2), 1989.
- 590 Bresson, E., Ducrocq, V., Nuissier, O., Ricard, D., and de Saint-Aubin, C.: Idealized numerical study of southern France
heavy precipitating events: Identification of favouring ingredients. Q. J. R. Meteorol. Soc., 138: 1751–1763, 2012.
- Carrió, D. S., Homar, V., Jansà, A., Romero, R. and Picornell, M. A.: Tropicalization process of the 7 November 2014
Mediterranean cyclone: numerical sensitivity study, Atmospheric Research, 197, 300–312, 2017.
- Chaboureau, J.-P., Pantillon, F., Lambert, D., Richard, E. and Claud, C.: Tropical transition of a Mediterranean storm by jet
595 crossing, Q. J. Roy. Meteorol. Soc., 138, 596–611, 2012.
- Cioni, G., Cerrai D., and Klocke D.: Investigating the predictability of a Mediterranean tropical-like cyclone using a storm-
resolving model, Q. J. Roy. Met. Soc., 144, 1598–1610, doi: 10.1102/qj.3322, 2018.
- Colella, P. and Woodward, P.R.: The Piecewise Parabolic Method (PPM) for Gas-Dynamical Simulations. Journal of
Computational Physics, 54, 174–201, [https://doi.org/10.1016/0021-9991\(84\)90143-8](https://doi.org/10.1016/0021-9991(84)90143-8), 1984.
- 600 Cuxart, J., Bougeault, P. and Redelsperger, J.L.: A turbulence scheme allowing for mesoscale and large-eddy simulations, Q.
J. Roy. Meteorol. Soc., 126, 1–30. <https://doi.org/10.1002/qj.49712656202>, 2000.
- D'Asaro, E. A., Sanford, T. B., Niiler, P. P., and Terrill, E.J.: Cold wake of Hurricane Frances. Geophys. Res. Lett., 34,
L15609, doi:10.1029/2007GL030160, 2007.
- Dafis, S., Rysman, J. F., Claud, C., and Flaounas, E.: Remote sensing of deep convection within a tropical-like cyclone over
605 the Mediterranean Sea. Atmospheric Science Letters, 19(6), e823, 2018.
- Di Muzio, E., Riemer, M., Fink, A. H., and Maier-Gerber, M.: Assessing the predictability of Medicanes in ECMWF
ensemble forecasts using an object-based approach. Q. J. R. Meteorol. Soc., 145(720), 1202–1217, 2019.
- Ducrocq, V., Nuissier, O., and Ricard, D.: A numerical study of three catastrophic precipitating events over southern France.
Part II: Mesoscale triggering and stationarity factors. Q. J. R. Meteorol. Soc. 134: 131–145, doi.org/10.1002/qj.199,
610 2008.
- Emanuel, K.A.: An air–sea interaction theory for tropical cyclones. Part I: Steady-state maintenance, J. Atmos. Sci., 43, 585–
604, 1986.
- Fita, L., and Flaounas, E.: Medicanes as subtropical cyclones: the December 2005 case from the perspective of surface
pressure tendency diagnostics and atmospheric water budget, Q. J. Roy. Meteorol. Soc., 144, 1028–1044, doi:
615 10.1002/qj.3273, 2018.
- Flaounas, E., Raveh-Rubin, S., Wernli, H., Drobinski, P. and Bastin, S.: The dynamical structure of intense Mediterranean
cyclones, Clim. Dynam., 44, 2411–2427, doi: 10.1007/s00382-014-2330-2, 2015.

- Flaounas, E., et al.: Assessment of an ensemble of ocean–atmosphere coupled and uncoupled regional climate models to reproduce the climatology of Mediterranean cyclones. *Clim. Dynam.*, 51(3), 1023–1040, 2018
- 620 Gaertner, M.A., Gonzalez-Aleman, J.J., Romera, R., Dominguez, M., Gil, V., Sanchez, E., Gallardo, C., Miglietta, M.M., Walsh, K., Sein, D., Somot, S., dell’Aquila, A., Teichmann, C., Ahrens, B., Buonomo, E., Colette, A., Bastin, S., van Meijgaard, E. and Nikulin, G.: Simulation of medicanes over the Mediterranean Sea in a regional climate model ensemble: impact of ocean-atmosphere coupling and increased resolution, *Clim. Dynam.*, 51, 1041–1057, 2017.
- 625 Gheusi, F., and Stein, J.: Lagrangian trajectory and air-mass tracking analyses with Meso-NH by means of Eulerian passive tracers, *Techn. Doc.*, http://mesonh.aero.obs-mip.fr/mesonh/dir_doc/lag_m46_22avril2005/lagrangian46.pdf, accessed on 18/02/2019, 2005.
- Hart, R.E.: A cyclone phase space derived from thermal wind and thermal asymmetry, *Mon. Weather Rev.*, 131, 585–616, 2003.
- 630 Homar, V., Romero, R., Stensrud, D.J., Ramis, C. and Alonso, S.: Numerical diagnosis of a small, quasi-tropical cyclone over the western Mediterranean: dynamical vs. boundary factors, *Q. J. Roy. Meteorol. Soc.*, 129, 1469–1490, 2003.
- Lac, C., Chaboureau, J.-P., Masson, V., et al.: Overview of the Meso-NH model version 5.4 and its applications, *Geosci. Model Dev.*, 1, 1929–1969, <https://doi.org/10.5194/gmd-11-1929-2018>, 2018.
- Lazar, A., Madec, G., and Delecluse, P.: The deep interior downwelling, the Veronis effect, and mesoscale tracer transport parameterizations in an OGCM. *J. Phys. Oceanogr.* 29 (11), 2945–2961. [https://doi.org/10.1175/1520-](https://doi.org/10.1175/1520-0485(1999)029<2945:TDIDTV>2.0.CO;2)
- 635 [0485\(1999\)029<2945:TDIDTV>2.0.CO;2](https://doi.org/10.1175/1520-0485(1999)029<2945:TDIDTV>2.0.CO;2), 1999.
- Lebeaupin Brossier, C., Arsouze, T., Béranger, K., Bouin, M.-N., Bresson, E., Ducrocq, V., Giordani, H., Nuret, M., Rainaud, R., and Taupier-Letage, I.: Ocean Mixed Layer responses to intense meteorological events during HyMeX-SOP1 from a high-resolution ocean simulation, *Ocean Model.*, 84, 84–103. <https://doi.org/10.1016/j.ocemod.2014.09.009>, 2014.
- 640 Lellouche, J.-M., Le Galloudec, O., Drévillon, M., Régnier, C., Greiner, E., Garric, G., Ferry, N., Desportes, C., Testut, C.-E., Bricaud, C., Bourdallé-Badie, R., Tranchant, B., Benkiran, M., Drillet, Y., Daudin, A., and De Nicola, C.: Evaluation of global monitoring and forecasting systems at Mercator Océan, *Ocean Sci.*, 9, 57–81, [https://doi.org/10.5194/os-9-57-](https://doi.org/10.5194/os-9-57-2013) 2013, 2013.
- Liu, W. T., Katsaros, K. B., and Businger, J. A: Bulk parameterization of air-sea exchanges of heat and water vapor including the molecular constraints at the interface, *J. Atmos. Sci.*, 36, 1722–1735, 1979.
- 645 Lyard, F., Lefevre, F., Letellier, T., and Francis, O.: Modelling the global ocean tides: modern insights from FES2004. *Ocean Dyn.*, 56 (5), 394–415. <https://doi.org/10.1007/s10236-006-0086-x>, 2006.
- Madec, G., and Imbard, M.: A global ocean mesh to overcome the north pole singularity. *Clim. Dyn.*, 12, 381–388, 1996.
- Madec, G., and the NEMO Team: NEMO ocean engine. Note du Pole de modélisation, Institut Pierre-Simon Laplace (IPSL), France, ISSN No 1288–1619. 27, 2016.
- 650 Masson, V., Le Moigne, P., Martin, E., Faroux, S., Alias, A., Alkama, R., Belamari, S., Barbu, A., Boone, A., Bouysse, F., Brousseau, P., Brun, E., Calvet, J.C., Carrer, D., Decharme, B., Delire, C., Donier, S., Essaouini, K., Gibelin, A.L., Giordani, H., Habets, F., Jidane, M., Kerdraon, G., Kourzeneva, E., Lafaysse, M., Lafont, S., Lebeaupin-Brossier, C., Lemsu, A., Mahfouf, J.-F., Marguinaud, P., Mokhtari, M., Morin, S., Pigeon, G., Salgado, R., Seity, Y., Taillefer, F., Tanguy, G., Tulet, P., Vincendon, B., Vionnet, V. and Voldoire, A.: The SURFEXv7.2 land and ocean surface platform for
- 655 coupled or offline simulation of Earth surface variables and fluxes, *Geosci. Model Dev.*, 6, 929–960, <https://doi.org/10.5194/gmd-6-929-2013>, 2013.

- McTaggart-Cowan, R., Davies, E. L., Fairman Jr, J. G., Galarneau Jr, T. J., and Schultz, D. M.: Revisiting the 26.5 C sea surface temperature threshold for tropical cyclone development. *Bull. American Meteorol. Soc.*, 96(11), 1929-1943, 2015.
- 660 Mesinger, F. and Arakawa, A.: Numerical Methods Used In Atmospheric Models, Global Atmospheric Research Program Publication Series 17(1), 1976
- Miglietta, M. M., Moscatello, A., Conte, D., Mannarini, G., Lacorata, G., and Rotunno, R.: Numerical analysis of a Mediterranean “hurricane” over south-eastern Italy: Sensitivity experiments to sea surface temperature, *Atmos. Res.*, 101, 412–426, 2011.
- 665 Miglietta, M.M., Laviola, S., Malvaldi, A., Conte, D., Levizzani, V. and Price, C.: Analysis of tropical-like cyclones over the Mediterranean Sea through a combined modelling and satellite approach, *Geophys. Res. Lett.*, 40, 2400–2405, 2013.
- Miglietta, M.M., Cerrai, D., Laviola, S., Cattani, E. and Levizzani, V.: Potential vorticity patterns in Mediterranean “hurricanes”. *Geophys. Res. Lett.*, 44, 2537–2545, 2017.
- Miglietta, M.M., and Rotunno, R.: Development mechanisms for Mediterranean tropical-like cyclones (medicanes), *Q. J. Roy. Meteorol. Soc.*, 1–17. <https://doi.org/10.1002/qj.3503>, 2019.
- 670 Morcrette, J.-J.: Radiation and cloud radiative properties in the ECMWF operational weather forecast model. *J. Geophys. Res.*, 96D, 9121-9132, 1991.
- Moscatello, A., Miglietta, M.M. and Rotunno, R.: Numerical analysis of a Mediterranean “hurricane” over southeastern Italy, *Mon. Weather Rev.*, 136, 4373–4397, 2008.
- 675 Myers, J. L., Well, A. D., and Lorch, R.F. Jr: Research Design and Statistical Analysis (3rd ed.), Taylor and Francis Eds., New York, 2010.
- Noyelle, R., Ulbrich, U., Becker, N., and Meredith, E. P.: Assessing the impact of sea surface temperatures on a simulated medicanes using ensemble simulations, *Nat. Hazards Earth Syst. Sci.*, 19, 941–955, <https://doi.org/10.5194/nhess-19-941-2019>, 2019.
- 680 Pergaud, J., Masson, V., Malardel, S. and Couvreux, F.: A parameterization of dry thermals and shallow cumuli for mesoscale numerical weather prediction, *Bound.-Layer. Meteor.*, 132, 83-106, doi: 10.1007/s10546-009-9388-0, 2009.
- Picornell, M. A., Campins, J., and Jansà, A.: Detection and thermal description of medicanes from numerical simulation, *Nat. Hazards Earth Syst. Sci.*, 14, 1059–1070, 2014.
- Pytharoulis, I.: Analysis of a Mediterranean tropical-like cyclone and its sensitivity to the sea surface temperatures. *Atmospheric Research*, 208, 167–179, 2018.
- 685 Rainaud, R., Lebeaupin Brossier, C., Ducrocq, V., and Giordani, H.: High-resolution air-sea coupling impact on two heavy precipitation events in the Western Mediterranean. *Quart. J. Roy. Meteor. Soc.*, 143, 2448–2462, <https://doi.org/10.1002/qj.3098>, 2017.
- Reale, O. and Atlas, R.: Tropical cyclone-like vortices in the extratropics: observational evidence and synoptic analysis. *Weather and Forecasting*, 16, 7–34, 2001.
- 690 Redelsperger, J.L. and Sommeria, G.: Three-dimensional simulation of a convective storm: Sensitivity studies on subgrid parameterization and spatial resolution, *J. Atmos. Sci.*, 43, 2619–2635, [https://doi.org/10.1175/1520-0469\(1986\)043<2619:TDSOAC.2.0.CO;2](https://doi.org/10.1175/1520-0469(1986)043<2619:TDSOAC.2.0.CO;2), 1986.
- Redelsperger, J.-L., Mahé, F. and Carlotti, P.: A simple and general subgrid model suitable both for surface layer and free-stream turbulence. *Bound.-Layer. Meteor.*, 101, 375–408. <https://doi.org/10.1023/A:1019206001292>, 2001.
- 695

- Reed, R.J., Kuo, Y.-H., Albright, M.D., Gao, K., Guo, Y.-R. and Huang, W.: Analysis and modeling of a tropical-like cyclone in the Mediterranean Sea, *Meteorol. Atmos. Phys.*, 76, 183–202, 2001.
- Renault, L., Chiggiato, J., Warner, J.C., Gomez, M., Vizoso, G. and Tintoré, J.: Coupled atmosphere-ocean-wave simulations of a storm event over the Gulf of Lion and Balearic Sea, *J. Geophys. Res.*, 117, C09019, doi:10.1029/2012JC007924, 2012.
- Ricchi, A., Miglietta, M.M., Barbariol, F., Benetazzo, A., Bergamasco, A., Bonaldo, D., Cassardo, C., Falcieri, F.M., Modugno, G., Russo, A., Sclavo, M. and Carniel, S.: Sensitivity of a Mediterranean tropical-like cyclone to different model configurations and coupling strategies, *Atmosphere*, 8(5), 92, 1–32, <https://doi.org/10.3390/atmos8050092>, 2017.
- Rotunno, R. and Emanuel, K.: An air–sea interaction theory for tropical cyclones. Part II: Evolutionary study using a nonhydrostatic axisymmetric numerical model. *J. Atmos. Sci.*, 44, 542–561, 1987.
- Roullet, G., and Madec, G.: Salt conservation, free surface and varying levels: a new formulation for ocean general circulation models. *J. Geophys. Res.* 105 (C10), 23927–23942. <https://doi.org/10.1029/2000JC900089>, 2000.
- Schade, L. R., and Emanuel, K. A.: The ocean’s effect on the intensity of tropical cyclones: Results from a simple coupled atmosphere–ocean model. *J. Atmos. Sci.*, 56, 642–651, 1999.
- Schär, C., and Wernli, H.: Structure and evolution of an isolated semi-geostrophic cyclone. *Q. J. R. Meteorol. Soc.*, 119(509), 57–90, 1993.
- Seity, Y., Brousseau, P., Malardel, S., Hello, G., Bénard, P., Bouttier, F., Lac, D. and Masson, V.: The AROME-France convective-scale operational model. *Mon. Weather Rev.*, 139, 976–991. <https://doi.org/10.1175/2010MWR3425.1>, 2011.
- Tibaldi, S., Buzzi, A. and Speranza, A.: Orographic cyclogenesis, in *Extratropical cyclones, The Palmen Memorial volume*, edited by: Newton, C., and Holopainen, E. O. American Meteorological Society, Boston, 107–127, 1990.
- Tous, M. and Romero, R.: Meteorological environments associated with medicane development, *Int. J. Climatol.*, 33, 1–14, 2013.
- Trenberth, K.: Uncertainty in hurricanes and global warming, *Science*, 308 (5729), 1753–1754, doi:10.1126/science.1112551, 2005.
- Voltaire, A., Decharme, B., Pianezze, J., Lebeaupin Brossier, C., Sevault, F., Seyfried, L., Garnier, V., Bielli, S., Valcke, S., Alias, A., Accensi, M., Arduin, F., Bouin, M.-N., Ducrocq, V., Faroux, S., Giordani, H., Léger, F., Marsaleix, P., Rainaud, R., Redelsperger, J.-L., Richard, E., and Riette, S.: SURFEX v8.0 interface with OASIS3-MCT to couple atmosphere with hydrology, ocean, waves and sea-ice models, from coastal to global scales, *Geosci. Model Dev.*, 10, 4207–4227, <https://doi.org/10.5194/gmd-10-4207-2017>, 2017.

Tables

	U_{10}	θ	SST	q
$H+LE$	0.66	-0.20	0.35	0.48
LE	0.65	0.10	0.36	0.33
H	0.38	-0.70	0.21	
U_{10}		-0.10	-0.25	0.84
θ			-0.04	-0.03
SST				-0.18

730 **Table 1:** Spearman's rank correlations between the enthalpy flux, latent and sensible heat flux and related parameters (10 m wind speed U_{10} , potential temperature at 10 m θ , SST and humidity at 10 m q) at 09:00 UTC on 7 November, from the CPL simulation, on the EF600 area.

	U_{10}	θ	SST	q
$H+LE$	0.62	-0.14	0.28	0.49
LE	0.49	0.22	0.42	0.23
H	0.55	-0.72	-0.10	
U_{10}		-0.19	-0.38	0.87
θ			0.41	-0.32
SST				-0.34

735 **Table 2:** Same at Table 1 at 13:00 UTC on 7 November.

	U_{10}	θ	SST	q
$H+LE$	0.31	-0.09	0.32	0.17
LE	0.16	0.26	0.46	-0.03
H	0.37	-0.75	-0.20	
U_{10}		-0.02	-0.52	0.93
θ			0.40	-0.04
SST				-0.49

Table 3: Same as Table 1 at 18:00 UTC on 7 November.

745

Figures

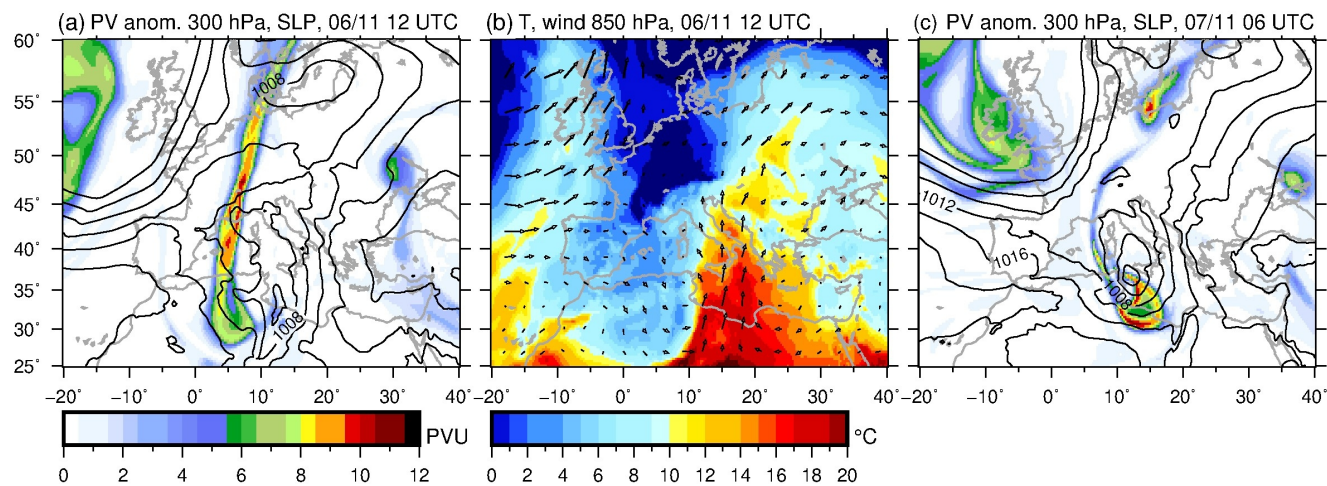


Figure 1: Potential vorticity (PV) anomaly at 300 hPa (colour scale) and SLP (isocontours every 4 hPa) at 12:00 UTC on 6 November (a) and 06:00 UTC on 7 November (c), temperature (colour scale, °C) and wind at 850 hPa at 06:00 UTC on 6 November (b) from the ERA5 reanalysis.

755

760

765

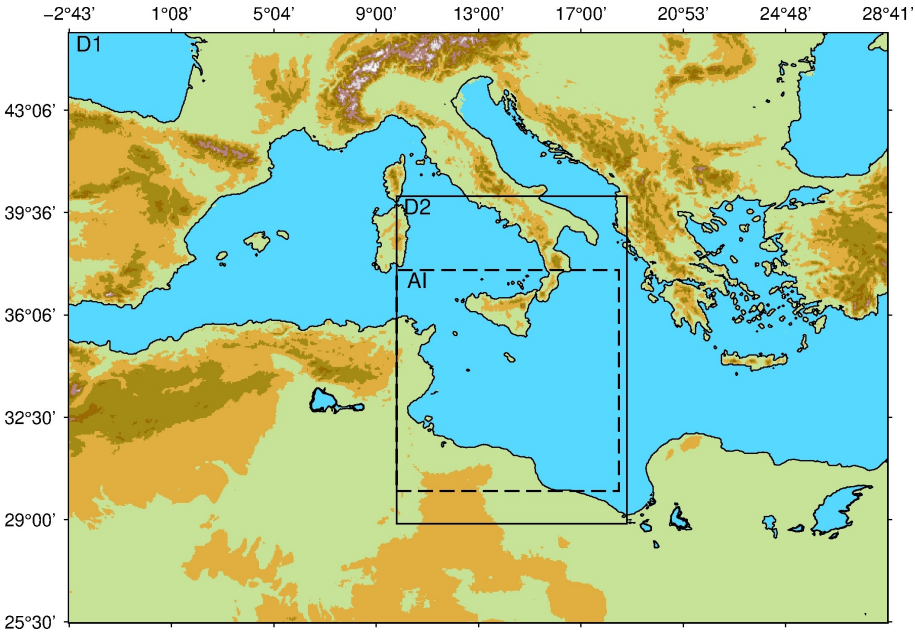


Figure 2: Map of the large-scale domain D1, with the domain D2 indicated by the solid-line frame and the area of interest (AI) indicated by the dashed-line frame.

775

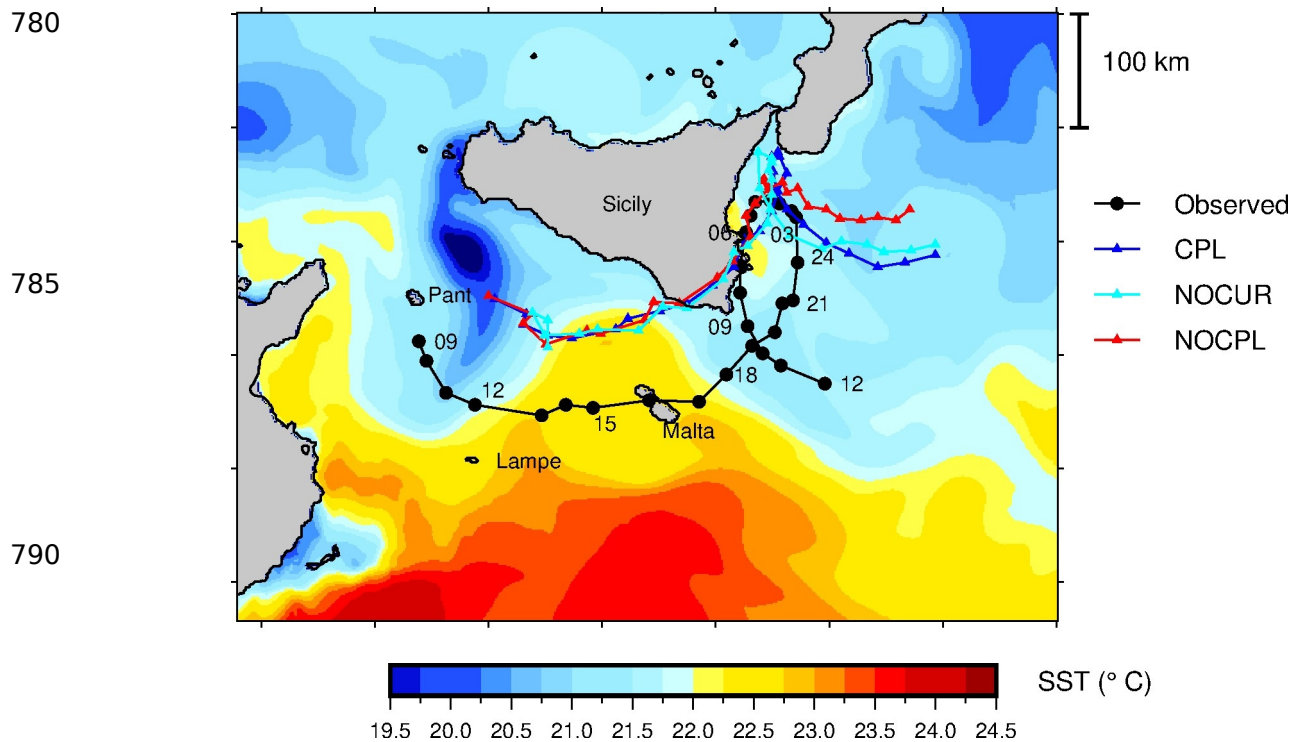


Figure 3: Comparison of the simulated tracks (triangles) of the non-coupled run (NOCPL, red), coupled run with SST only (NOCUR, cyan) and fully coupled run (CPL, blue) with the best track (black closed circles) based on observations as in Cioni et al., (2018). The position is shown every hour with time labels every 3 h, starting at 09:00 UTC on 7 November until 12:00 UTC on 8 November. In colours, initial Sea Surface Temperature (SST, °C) at 01:00 UTC on 7 November.

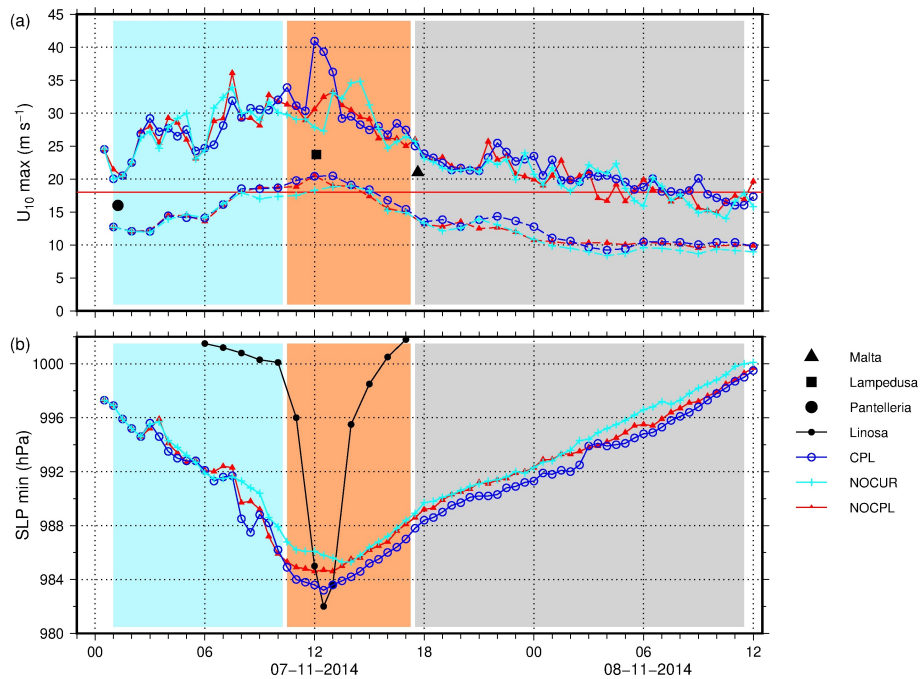


Figure 4: Time series of the maximum of the 10 m wind speed, and 10 m wind averaged over a 100 km radius around the cyclone centre (a) and minimum sea-level pressure (b) as obtained in the different simulations on the 7 November and 8 November until 12:00 UTC. The thin red line in (a) indicates the 18 m s^{-1} wind speed threshold. The background shading (here and in the following time-series plots) indicates the development (light blue), mature (orange) and decay (grey) phases. The observations of SLP in Linosa (black plain circles) are shown for comparison in (b), the observations of wind speed from Malta, Lampedusa and Pantelleria are shown in (a) – see text.

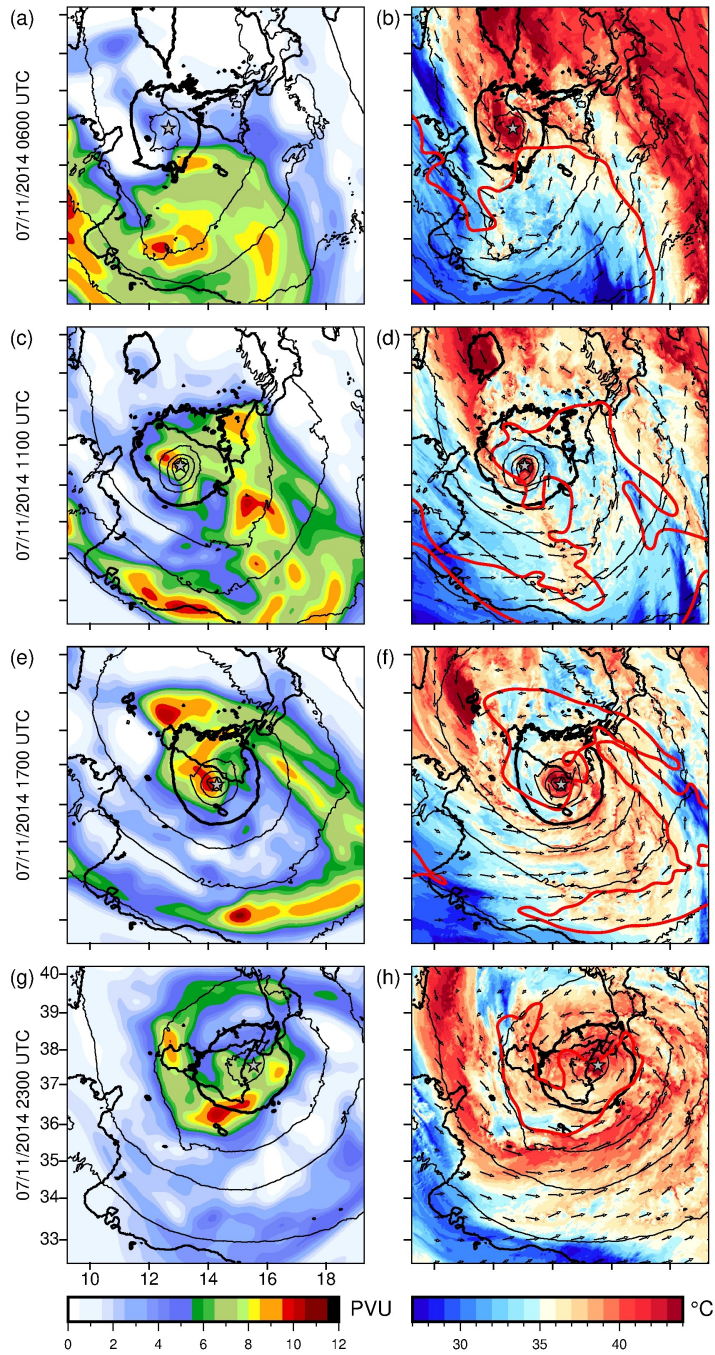


Figure 5: Potential vorticity at 300 hPa (colour scale) and SLP (isocontours every 4 hPa, the 1000 hPa isobar is in bold), (a, c, e, g) and equivalent potential temperature ($^{\circ}\text{C}$, colour scale) and wind at 850 hPa, SLP, and 6 PVU at 300 hPa isocontours (red), (b, d, f, h) from the NOCPL simulation.

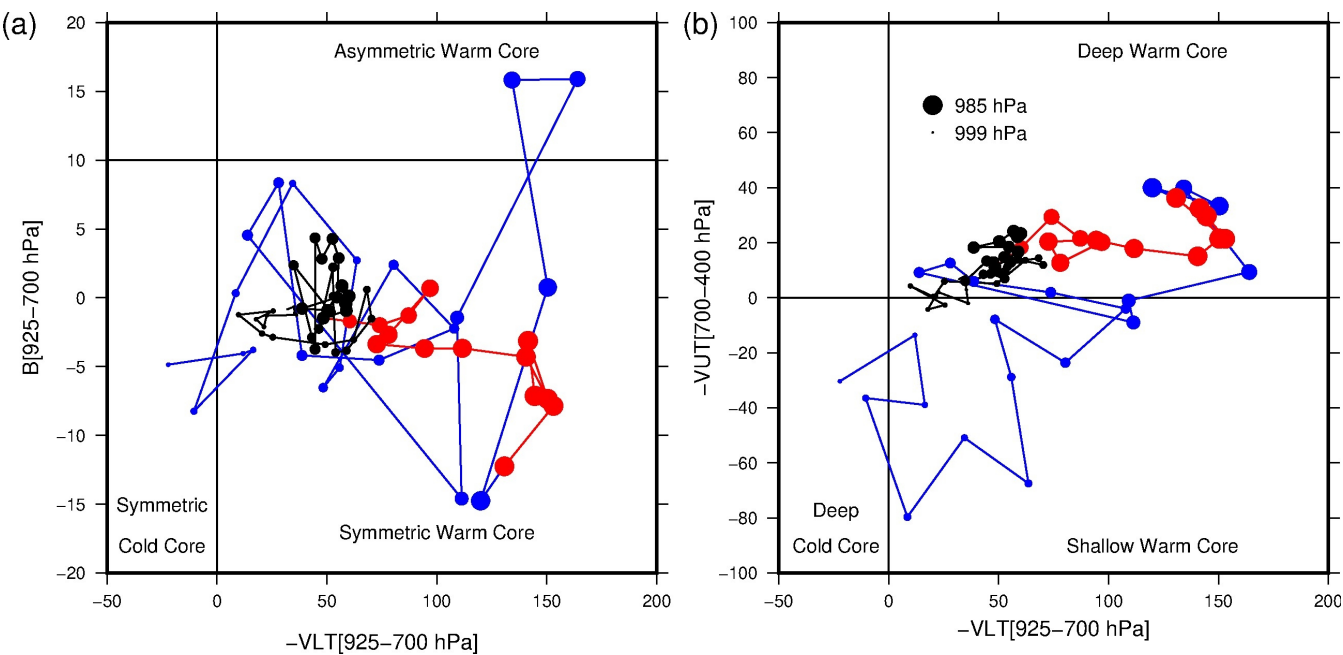


Figure 6: Phase diagram of the NOCPL simulated cyclone from 01:00 UTC on 7 November till 12:00 UTC on 8 November, with low-tropospheric thickness asymmetry inside the cyclone (B) with respect to low-tropospheric thermal wind ($-V_{LT}$) (a), and upper-tropospheric thermal wind ($-V_{UT}$) with respect to low-tropospheric thermal wind (b). The development phase is in blue, the mature phase in red, and the decay phase in black.

875

880

885

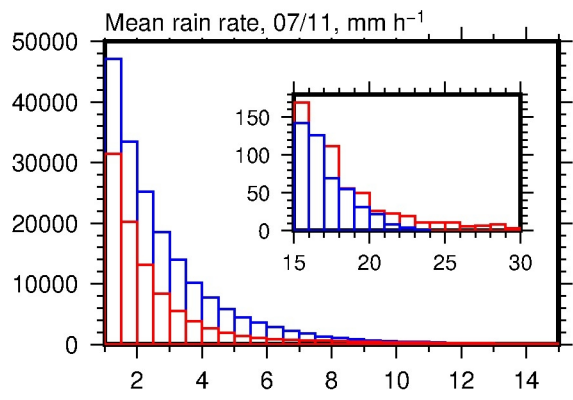


Figure 7: Histogram of the mean rain rate distribution (in number of grid points) for the development (blue) and mature (red) phases in the NOCPL simulation. The enclosed figure shows a zoom on the highest rates.

890

895

900

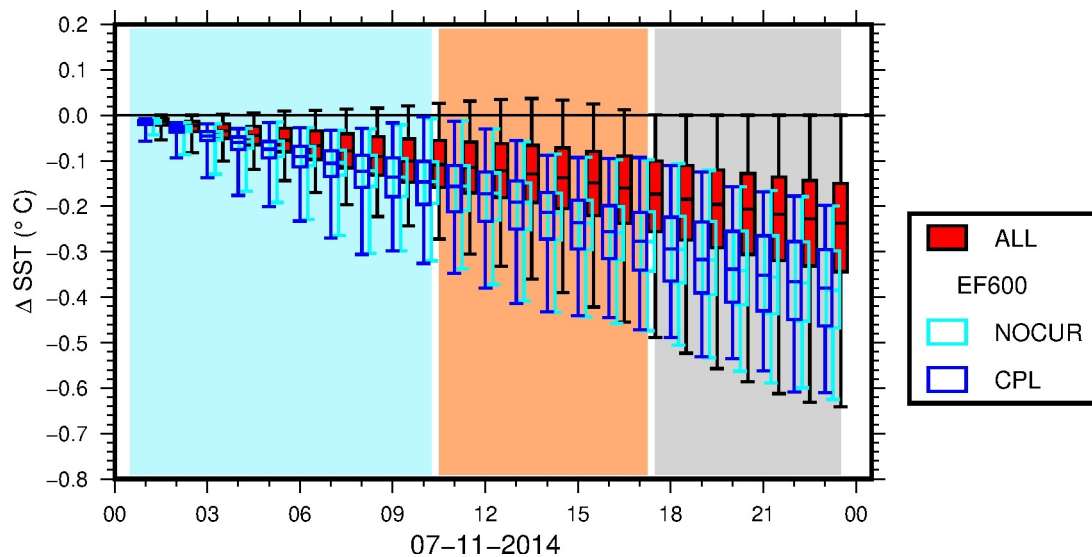


Figure 8: Time series of the median differences between the SST in the CPL and NOCPL simulations, on the whole domain (red) and on the EF600 area (blue, see text for definition), on the 7 November. The boxes indicates the 25 and 75% quantiles and the whiskers the 5 and 95% quantiles. Are also shown the differences between the NOCUR and NOCPL simulations (cyan). Some of the boxes have been slightly shifted horizontally for clarity.

905

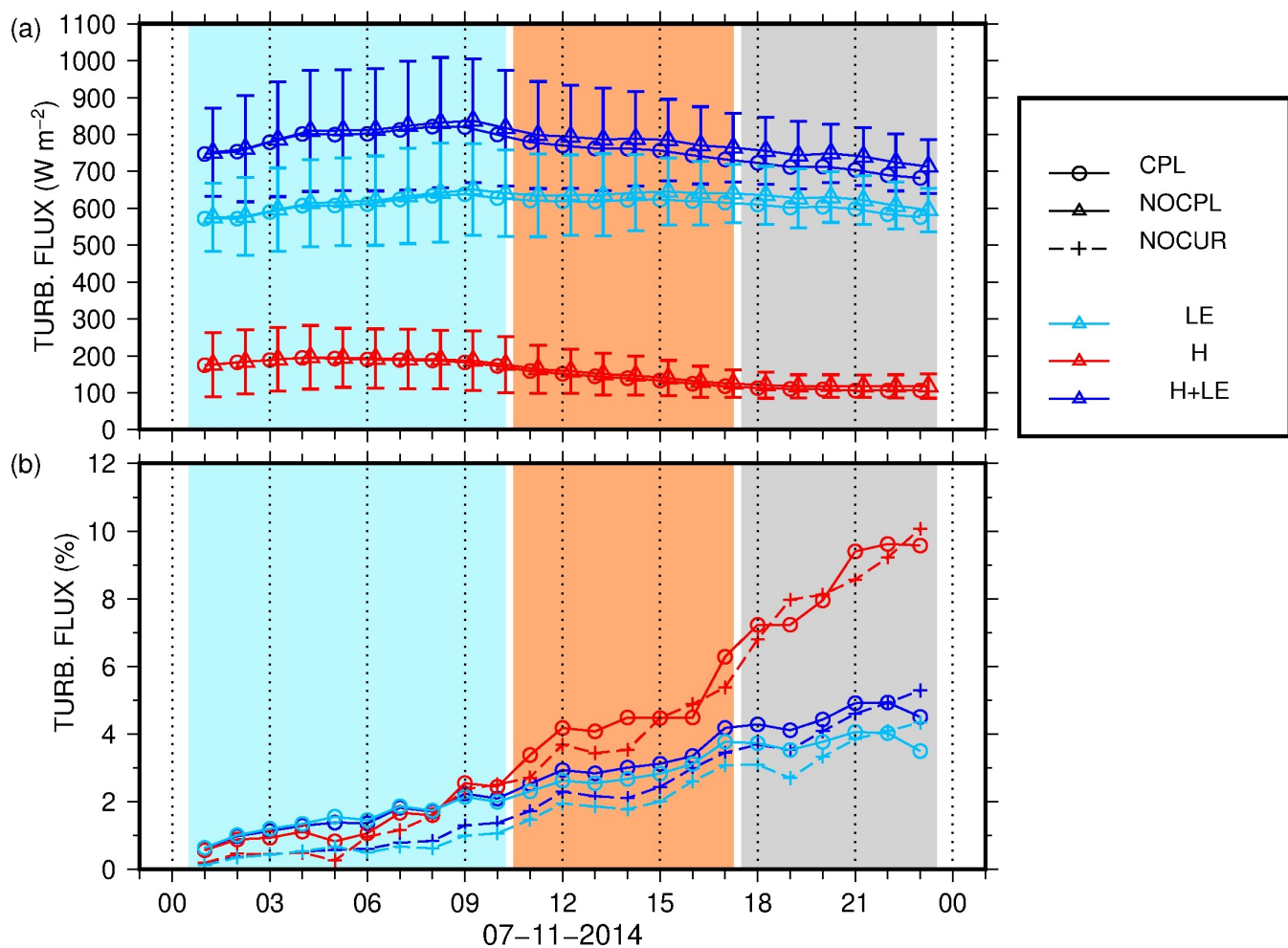


Figure 9: Time series of the mean values and standard deviation (error bars) of the total turbulent heat flux (blue), latent (cyan) and sensible heat flux (red) in the CPL (open circles) and NOCPL (triangles) simulations (a) and of the mean difference between CPL and NOCPL turbulent fluxes (open circles, same colour code) and between NOCUR and NOCPL turbulent fluxes, in percent relative to the NOCPL values (b) on the EF600 area.

920

925

930

935

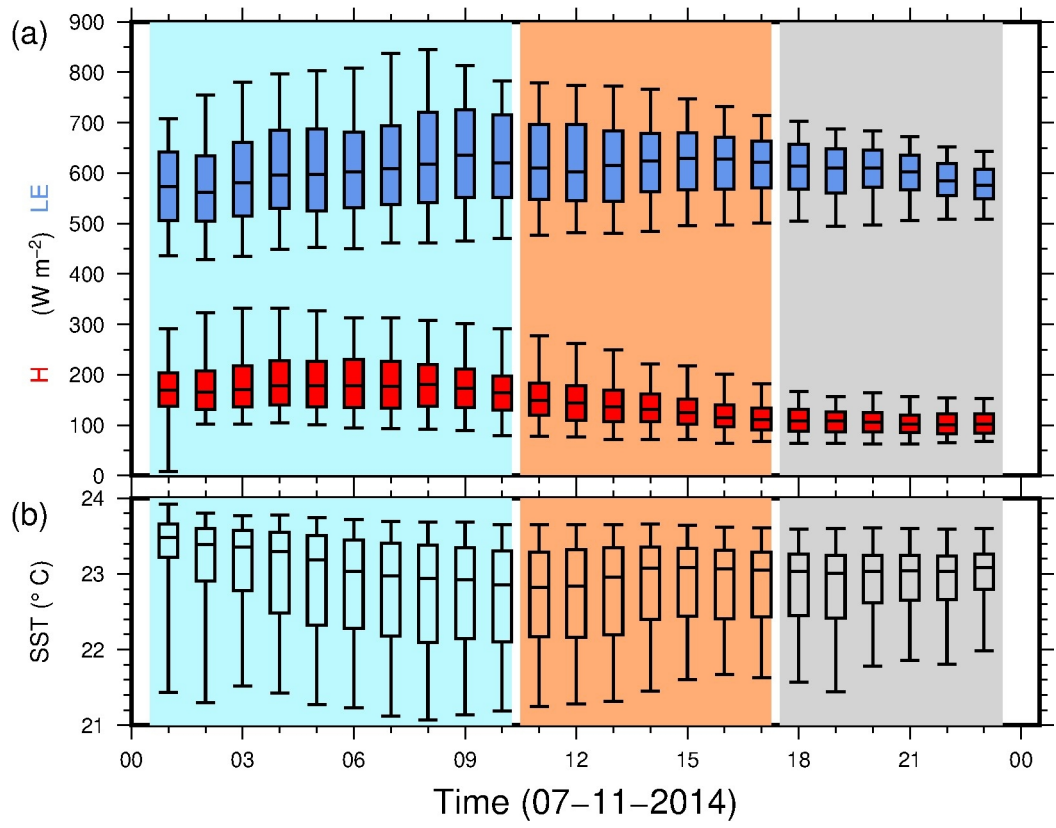


Figure 10: Time series of the median values of latent (blue) and sensible heat fluxes (red, a) and of SST (b) on the EF600 area (see text) on the 7 November. The boxes corresponds to the 25 and 75% quantiles, the whiskers to the 5 and 95% quantiles.

940

945

950

955

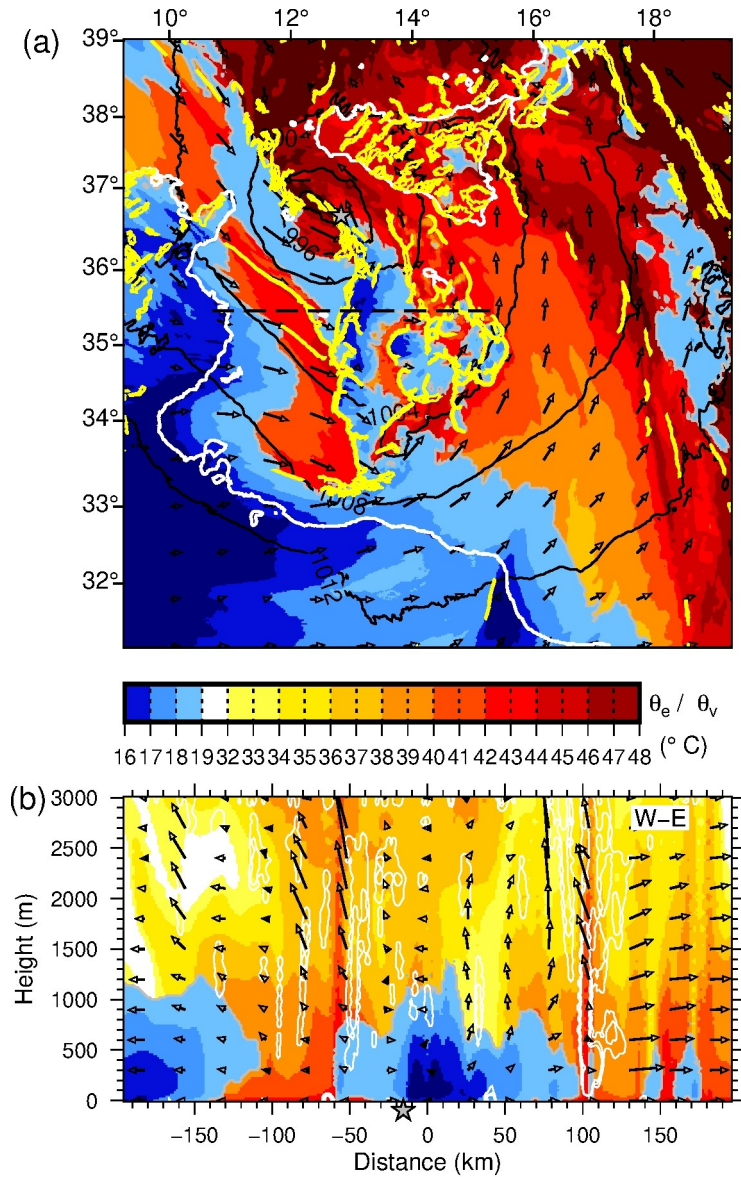


Figure 11: Map of equivalent potential temperature (warm colors) and virtual potential temperature below 19 °C (blue shades), horizontal convergence rate above $1 \times 10^{-3} \text{ m s}^{-2}$ (yellow contours), 10 m wind (arrows) and SLP (black contours) at 08:30 UTC on 7 November (a), and vertical cross-section of equivalent potential temperature and virtual potential temperature (colour scale), tangential wind (black vectors, the vertical component is amplified by a factor 20), potential vorticity anomaly (white contour at 5 PVU) along a west-east transect (b) (dashed line in (a)). The grey stars indicate the position of the SLP minimum.

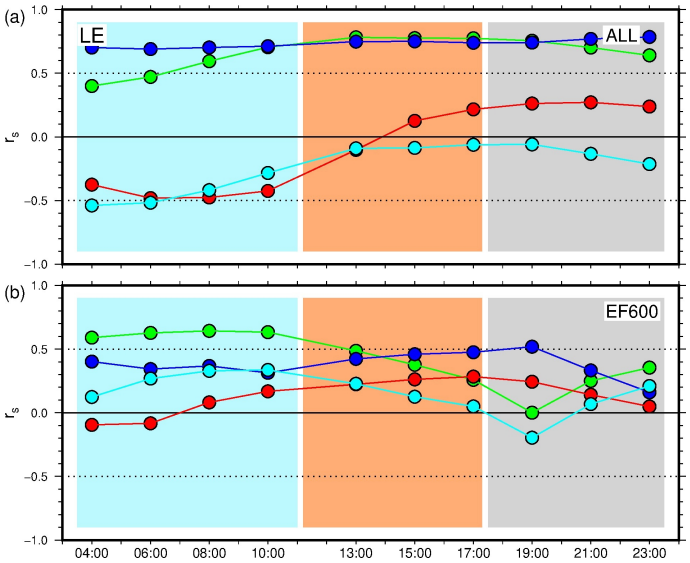


Figure 12: Time series of Spearman's rank-order correlation r_s between the latent heat flux LE and 10 m wind speed (green), potential temperature at 10 m (red), SST (blue) and specific humidity at 2 m (cyan) on the whole domain (a) and EF600 area (b), in the CPL simulation.

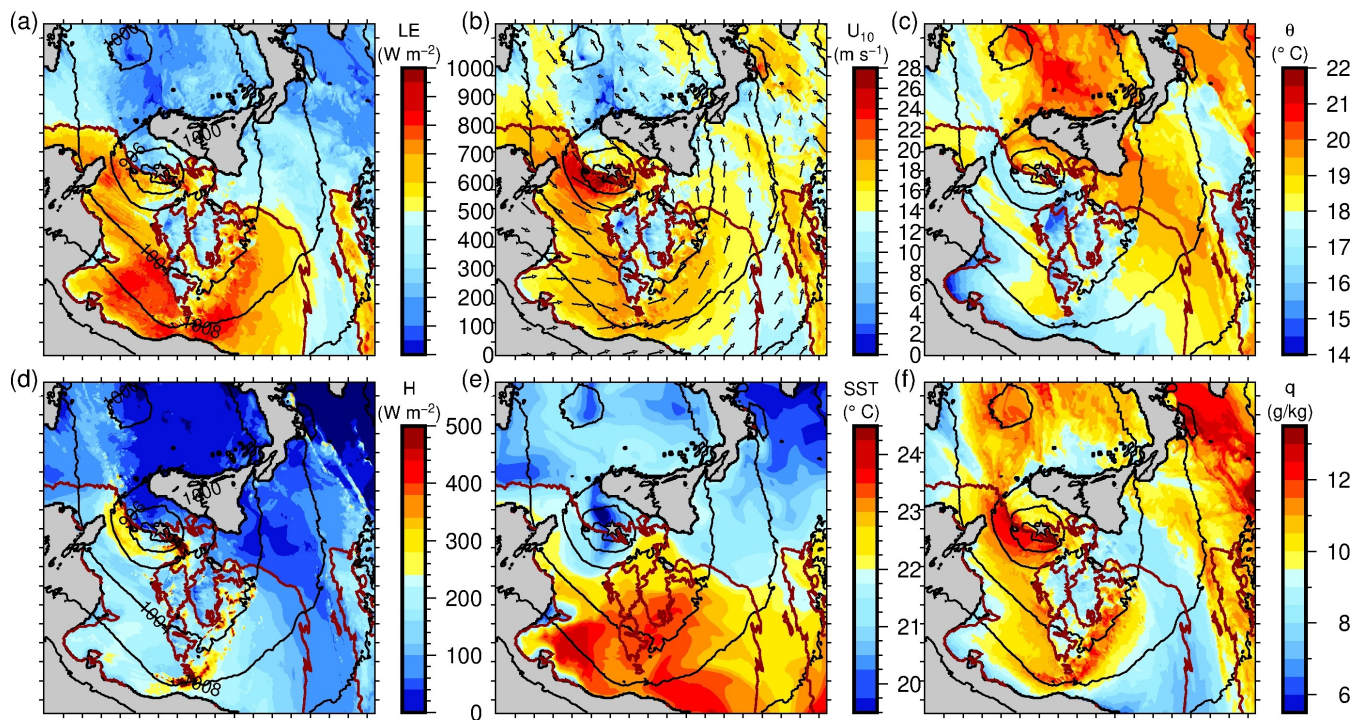
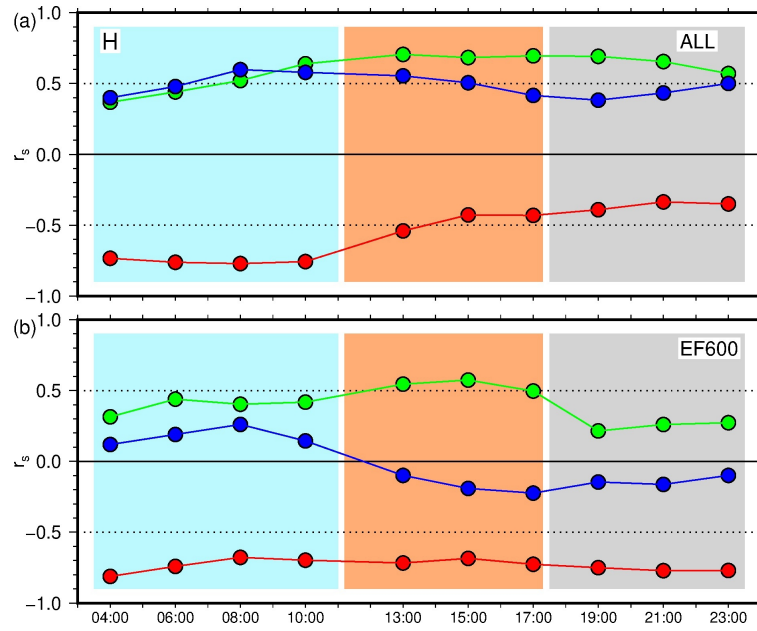


Figure 13: Maps of the total turbulent heat fluxes LE (a), H (b), the 10 m wind U_{10} (c), the 10 m potential temperature (d), the SST (e) and the specific humidity at 2 m (f) at 09:00 UTC on 7 November, in the CPL simulation.

1010



1015

Figure 14: Same as Figure 12 but between the sensible heat flux H and 10 m wind speed (green), potential temperature at 10 m (red), and SST (blue) on the whole domain (a) and EF600 area (b), in the CPL simulation.

1020

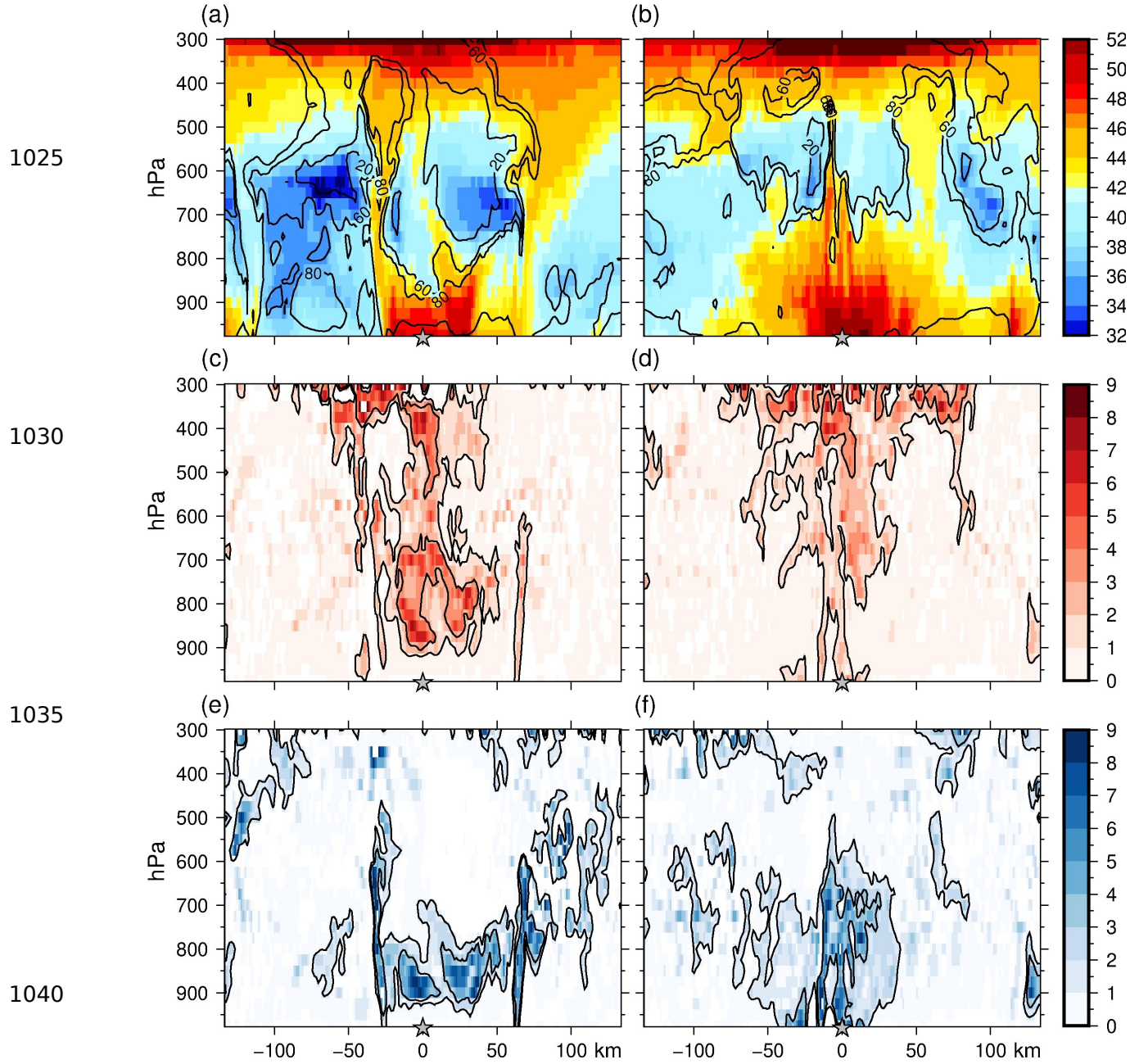


Figure 15: Vertical cross-sections of equivalent potential temperature θ_e ($^{\circ}\text{C}$, colour scale) and relative humidity (%), (a,b), DPV (intensity), (c,d) and WPV (intensity), (e,f) on a west-east transect across the cyclone centre, at 13:00 (a,c,e) and 18:00 UTC (b,d,f) on 7 November, in the CPL simulation. The black contours in (c) to (f) correspond to intensities 1 and 3 (as defined in Miglietta et al., 2017).

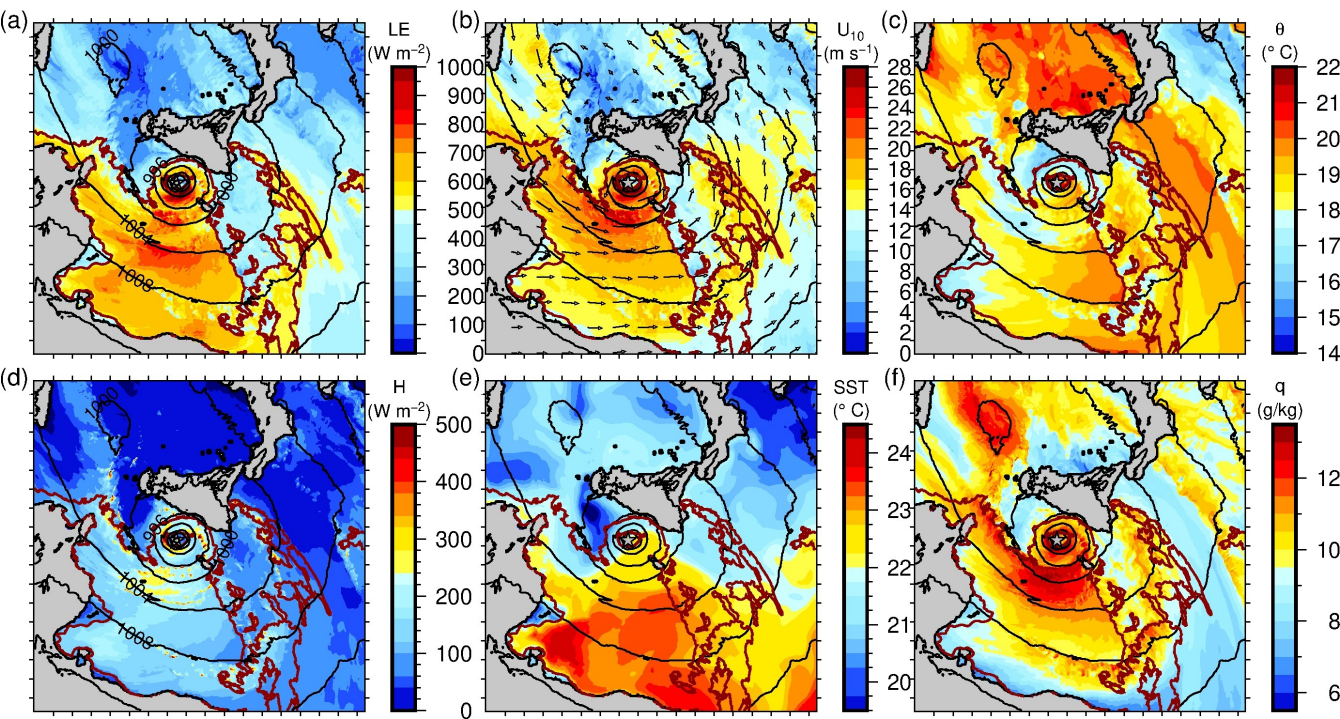


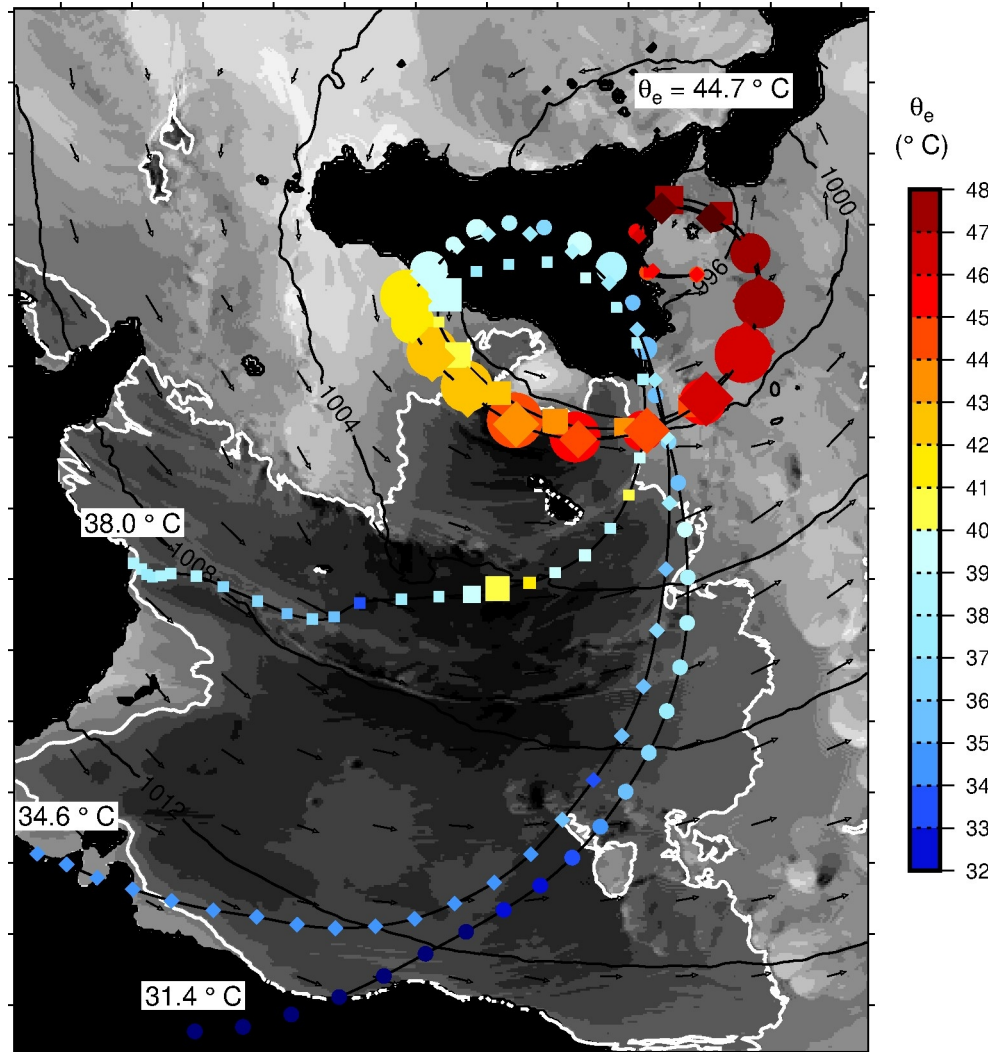
Figure 16: Same as Figure 13 but at 13:00 UTC on 7 November.

1055

1060

1065

1070



1075

Figure 17: Map of the backtrajectories of air parcels arriving south of the cyclone centre at 23:00 UTC on 7 November, 1500 m above sea level, at 3 different levels (circles, squares and diamonds). The first point of the trajectories correspond to the start of the D2 domain simulation (00 UTC the 07 November). The colour scale indicates the equivalent potential temperature ($^{\circ}\text{C}$) and the size of the symbol is inversely proportional to altitude between 0 and 1000 m. Are also shown the values of the final equivalent potential temperature, of the initial equivalent potential temperatures, the wind field at 900 hPa (black vectors), and the surface enthalpy flux (grey shades) with a threshold at 600 W m^{-2} (white contour) at 15:30 UTC when the particles arrive at sea south of Sicily.

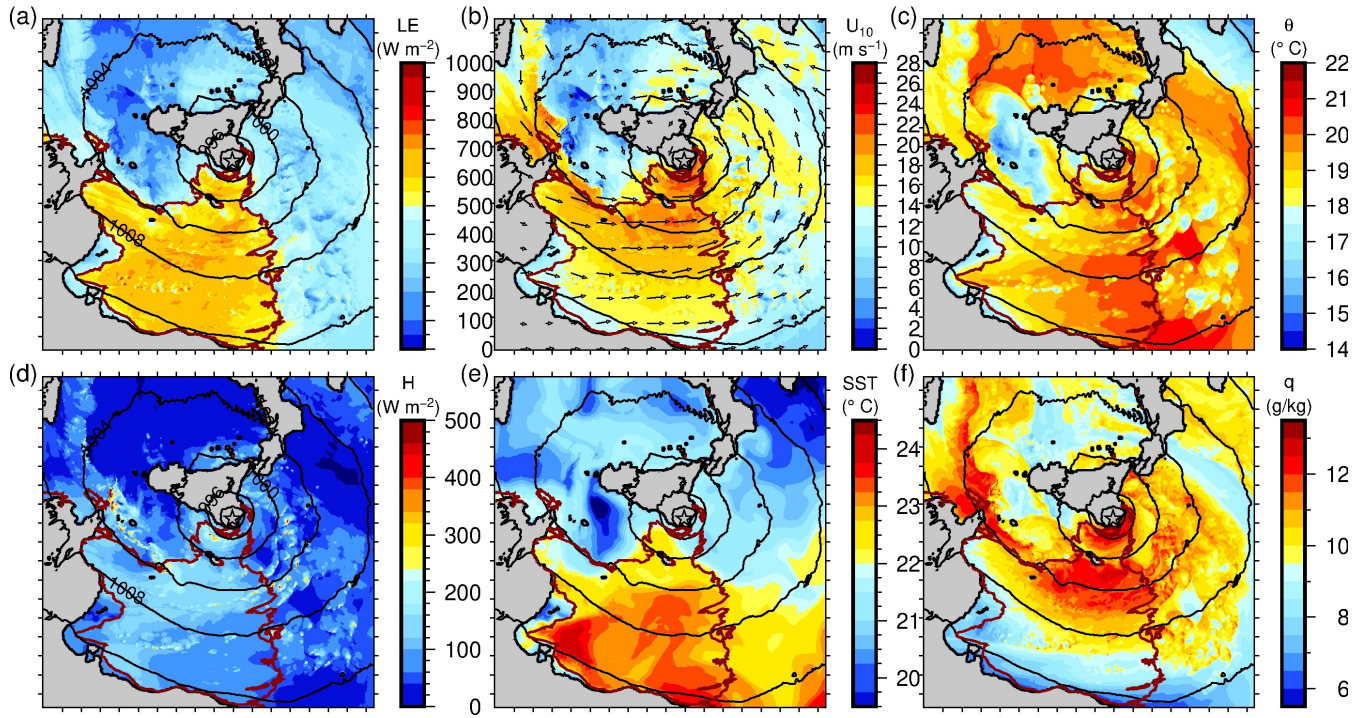


Figure 18: Same as Figure 13 but at 18:00 UTC on 7 November.

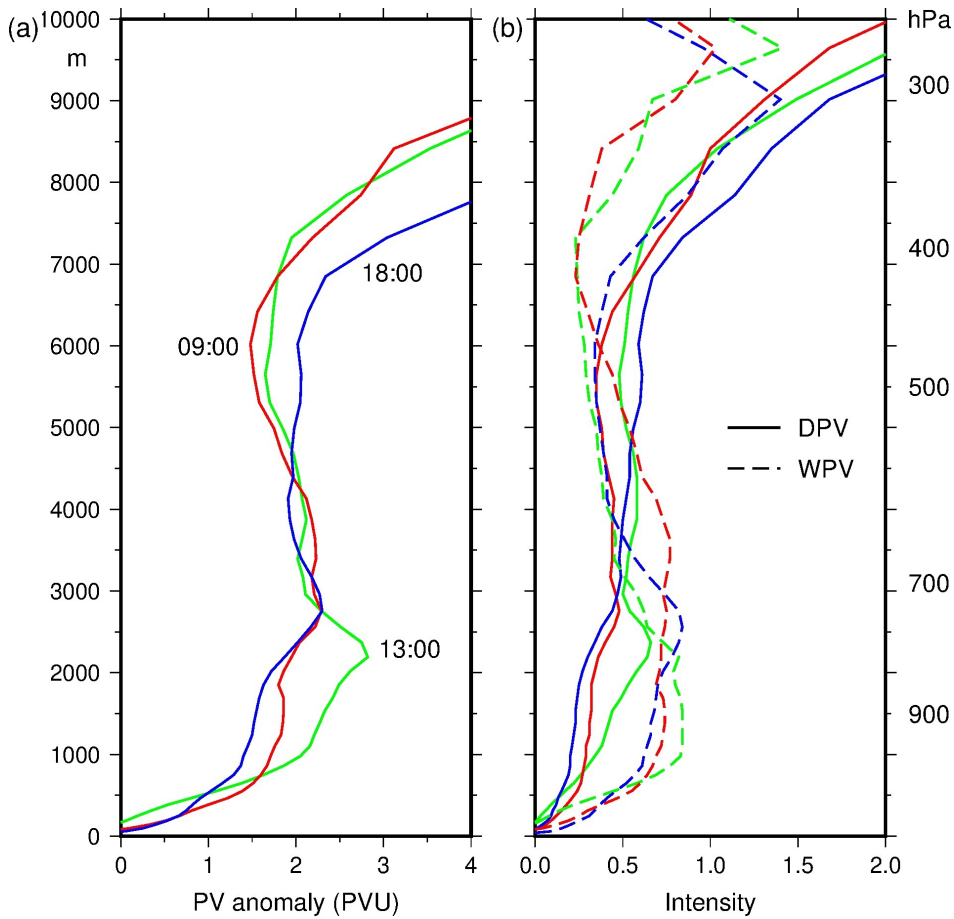


Figure 19: Vertical profiles of PV (a), and DPV and WPV (b) averaged within a 100-km radius circle around the cyclone centre at 09:00 (red), 13:00 (green) and 18:00 UTC (blue) on 7 November, in the CPL simulation.